CORUS: Cryo bio-nano-imaging beamline

Proposer Team:

José Javier Conesa (CNB-CSIC, Spain) (SP)

Carlos Sánchez-Cano (DIPC, Spain) (SP)

Daniel Chevrier (CEA, France)

Carles Bosch (Francis Crick Institute, UK) (SP)

Eva Pereiro (ALBA, Spain)

Alessandra Patera (ALBA, Spain)

Judith Juanhuix (ALBA, Spain)

Alberto Mittone (APS, USA)

Frédéric Jamme (SOLEIL, France)

Emil Malucelli (University of Bologna, Italy)

Contents

1. Scientific cases

Executive summary

Despite advancements in nano-biotechnologies, understanding complex biological systems, diseases and environmental problems requires new scientific strategies and tools to gain structural, chemical and elemental knowledge at the nanoscale and in close-to-native conditions. Scientific progress is often limited by our inability to capture and understand biological or environmental systems in a representative state with adequate combination of spatial and spectral resolutions. Toward this aim, a hard X-ray cryogenic nanoprobe is an essential and versatile instrument to investigate sensitive biological samples, such as mammalian cells or tissues, at the nanoscale, to understand their structure and interactions at the bio-nano interface.

Cryo nano-scanning X-ray fluorescence and spectroscopy are quantitative techniques that can reveal the subcellular distribution of oligoelements (*e.g.*, N, P, Ca or S), related to the metabolic role and state of organelles[1], and the oxidation state of trace-level metals (*e.g.*, Fe, Mn, Cu or Zn), relevant to a plethora of tightly regulated biochemical functions maintaining cellular homeostasis[2]. The role of metals involved in parasitic and viral infections, cancer and neurodegenerative diseases can also be investigated with these nanoprobe techniques[3]. The performance and degradation of engineered metal-based drugs or nanoparticle delivery vehicles (*e.g.*, Ag and Au) can also be evaluated by determining their intracellular location along with chemical and structural changes from their therapeutic action[4]. Equally important is to understand the fate and effect of human-engineered nanomaterials released into the environment[5]. From a bottom-up point of view, investigating the formation of biologically-synthesized minerals and materials at early stages can reveal key structural and chemical controls that living systems have over their intracellular and local environment. Such information is pertinent to understanding biomineralization pathways from mammalian cells (*e.g.*, bone) down to single bacteria (*e.g.*, magnetic nanoparticles). In addition to fluorescence and spectroscopic techniques, X-ray phase-contrast imaging can be measured simultaneously and provide details on the complex structural organization of biological materials, such as tissues, with insights on the subcellular morphology. Examples of applying nano-scanning X-ray phase contrast methods are the 3D mapping of brain tissue from neuron cell structure up to the local organization of neuronal connections and the hierarchical structure of bone, with its response to injury and implant, among others. Understanding these intricate and highly-ordered structures at different scales is crucial for developing effective treatments and preventative strategies to improve human health.

Overall, cryo nano-scanning X-ray imaging and spectroscopy techniques employed at a hard X-ray nanoprobe can offer immediate structural and chemical insights on a range of biological systems. These results can help Academia and Industry researchers to tackle urgent scientific questions and societal concerns from Health to the Environment, such as metallomics, pathogen-host interactions, metal nanocomposites, toxicology, tissue organization, biomineralization, bioremediation strategies, food security and sustainable agriculture, among others. This research diversity is in line with the ***One Health*** concept, as defined by the World Organisation for Animal Health, for which humans, animals and plant health are interdependent and bound to the health of the ecosystems in which they exist.

Metallomics

Metal ions take part in biological processes in all forms of life. They have unique chemical and physical properties that allow them to provide crucial biochemical activities and structural motifs to cellular components [1]. To better understand the biology of the cell, it is necessary to have access to the intracellular space to reveal the elemental composition, quantity and distribution of molecules and elements. Bulk methods are able to provide average information of several cells but lack the intrinsic

variability of cell phenotypes. Studying metals within the subcellular space with sufficient spatial resolution can help decipher the biochemical state of the cell, offering a means to address many biological questions.

The importance of metallomics in biological processes is evident for the case of neutrophils. Once a bacterial or fungal pathogen penetrates into tissue it is sensed by cells that send a recruiting signal for neutrophils. Neutrophils migrate to the infection site quickly and accumulate in high numbers. Once at the infection site, neutrophils recognise the pathogen and fight them by phagocytosis, intra- and extracellular toxification, and local retainment[2]. In the work of Niemiec and collaborators[3] an in-depth XRF analysis of trace elements of human neutrophils revealed that they present a cell type-specific composition of Zn, Fe, Cu and Mn with an exceptionally high Fe content that could be related to a specific enzyme profile, and hence to their role in the immune reaction. They characterized the elemental composition of neutrophil extracellular traps (NETs), which are extracellular networks with antimicrobial activity formed by neutrophil content released in a controlled cell death process called NETosis. They found that NETs are able to chelate Zn, thereby lowering its concentration, which could lead to Zn microbial pathogen starvation (nutritional immunity). However, these experiments were performed on lyophilized samples. **An elemental study under cryogenic conditions combined with phase contrast imaging, as would be provided by CORUS, would offer closer to native-state conditions and consequently a more precise evaluation of the chemical profile of neutrophils.**

Pathogen-host interaction

With infectious disease epidemics becoming more frequent and spreading faster in various regions of the world, the resulting impact on health and economic systems have become increasingly significant. Taking this into account, it is essential to develop rapid diagnostic tools and effective control strategies for epidemic prevention[4] but also to characterize the pathogen-host interaction.

Trace elements have important roles in **viral infection**, they are involved in the attachment of the virus to host membranes[5] and its homeostasis deregulation is characteristic of viral infection[6]. For example, Fe, Cu or Zn are known to bind to proteins implicated in viral infection[7]. Zn is required for the normal development and function of the organism. It is associated in gene expression, as cofactor in enzymes and in the immune response[8]. Studies have reported the relationship between Zn and viral infections[9]. For instance, a Zn deficit has been shown during HIV infection, hepatitis and tuberculosis indicating that low Zn levels in the organism increase susceptibility to viral infection[10]. Zn has an effect on viral replication and in viral adhesion, infection or uncoating[11]. Fe is fundamental in several host and viral functions. It is involved in DNA replication and cellular proliferation and its imbalance can increase susceptibility to viral infection[12]. For example, elevated Fe levels are associated with the progression of hepatitis virus infection[13]. Cu balance is tightly related to the Fe homeostasis[14] and its dysregulation can affect normal cellular functions, posing an increased sensitivity to viral infections. Cu is implied in viral entry and replication inhibition, and in viral mRNA and capsid protein degradation[15]. Most of the knowledge on the metallome during viral infection is derived from approaches different from XRF, such as inductively coupled plasma mass spectrometry (ICP-MS), laser ablation coupled to ICP-MS (LA-ICP-MS) or secondary ion mass spectrometry (SIMS). **The study of metal distribution in pathogen-host interactions would greatly benefit from CORUS, with its high sensitivity, resolution, 3D imaging capabilities and the possibility of analyzing samples in a hydrated state.**

Microbial infections, those caused by bacteria or parasites, are also linked to metal homeostasis. Metal availability induces a selective pressure at the pathogen-host interaction that causes an evolutionary arms race to generate different metal sequestration strategies[16]. In bacterial infections, understanding the role of metals is critical to identify novel therapeutic targets (nutritional immunity-based therapeutics)[17].

Wagner and collaborators[18] studied the distribution of elements inside macrophages during the infection of *Mycobacterium spp*. XRF revealed the elemental composition of infected macrophage phagosomes containing *Mycobacterium*, showing an increased amount of Fe within them. Additionally, it was observed that Fe depletion in macrophages leads to attenuated intramacrophage survival of the pathogen, indicating that Fe sequestration could be a potential therapeutic target. All these experiments were carried out in dried samples and with micrometer resolution. **CORUS could be used to provide higher resolution and sensitivity of the elemental distribution in a cellular context and in cryogenic conditions, which would render more precise and truthful information on the implication of metal homeostasis during viral infection.**

A relevant example in **parasite infection** is the case of *Plasmodium falciparum*. Its asexual life cycle occurs inside human red blood cells. There, it metabolizes haemoglobin to grow and spawn into a new generation of parasites that are able to infect new red blood cells, causing malaria disease. As a result of the degradation of haemoglobin, heme is generated. This metabolite is toxic for the parasite in solution so it has developed mechanisms to precipitate it into hemozoin crystals, a non-toxic compound for the parasite[19]. In the work of Kapishnikov and collaborators[20] a combination of cryo Soft X-ray Tomography (SXT), to provide the cell ultrastructure, and 2D XRF, to map the distribution of elements as K, S and Fe, was used to analyse *P. falciparum* infected red blood cells. They determined that the ratio between Fe and S in different compartments of the cell can give information about the proportion of the different haemoglobin metabolites, which can be related to the stage of the parasite's asexual cycle (i.e., *in situ* biochemistry). This could reveal details of the parasite's asexual multiplication, leading to more intelligent designs of drugs to disrupt it. **CORUS could be used to generate information similar to that provided by Kapishnikov and collaborators, producing the elemental and ultrastructural information of the same cells using a single microscope, simplifying the correlative workflow.**

Another important threat to public health is the spread of **antibiotic-resistant bacteria**, leading to incurable infections. Evidently, the pace of new antibiotics discovery to fight these pathogens has substantially slowed, possibly due to the many gaps remaining in our knowledge of antibiotics. For example, it is unclear why some compounds penetrate into bacterial cells and others not, and even how some can breach the more restrictive envelope of Gram-negative species. Indeed, the presence of an effective penetration barrier in bacteria and the paucity of novel penetrating compounds are two main limiting issues responsible for the lack of progress in the field of antibacterial research.

As stated above, metals such as Fe or Zn play important functions in bacterial physiology, thus drugs that target their uptake or downstream utilization represent a promising approach. Recently, metals gained considerable attention as potential antimicrobials[21]. Good examples are "Trojan horse" metallophores linked to antibiotics that divert specific Fe-siderophore transporters (i.e., FDA-approved Cefiderocol) and Zn chelators that inhibit metallo-β-lactamases. Metal complexes stand out as potential agents as their properties can be manipulated in ways similar to those used in conventional drug development. In addition to the rich structural diversity of metal complexes, these also have access to a range of multiple mechanisms of action, a common point being oxidative stress. In this direction, Mark Blaskovich team (Center for Superbug Solutions, The University of Queensland, Australia) is housing the Community for the Open Antimicrobial Drug Discovery(CO-ADD) platform and has already screened over 295,000 compounds, including 1,000 metal complexes. A recent analysis of CO-ADD revealed that metal complexes display hit rates against problematic bacterial pathogens 10 times higher than organic molecules[21].

Early approaches using fluorescent antibiotics and deep UV (DUV) spectromicroscopy enabled a major advance in the quantification of antibiotic accumulation in bacterial populations down to the scale of the single bacterium[22-27]. Several studies have highlighted the molecular determinants underlying the

accumulation of fluoroquinolones (FQs) in *Escherichia coli* as a model for Gram-negative bacteria. It has been demonstrated that the main AcrAB-TolC efflux pump controls the accumulation kinetics of FQs, relative to the level of bacterial resistance to this family of antibiotics[28, 29]. However, the limited resolution of DUV microscopy and the lack of DUV-fluorescence calibration impairs the possibility to obtain precise subcellular localization and intracellular quantification of FQs into single bacterial cells. The recent use of metallo-FQs[30] and cryo-nano-XRF have made it possible to circumvent this limitation (Jamme & Masi, unpublished data). **Antibiotic resistance research will be undoubtedly strengthened thanks to the possibility of correlative 3D cryo-nanoimaging at CORUS [31] (see Fig. 1), providing quantification and localization of promising metallo-antibiotics at subcellular resolution of bacteria.**
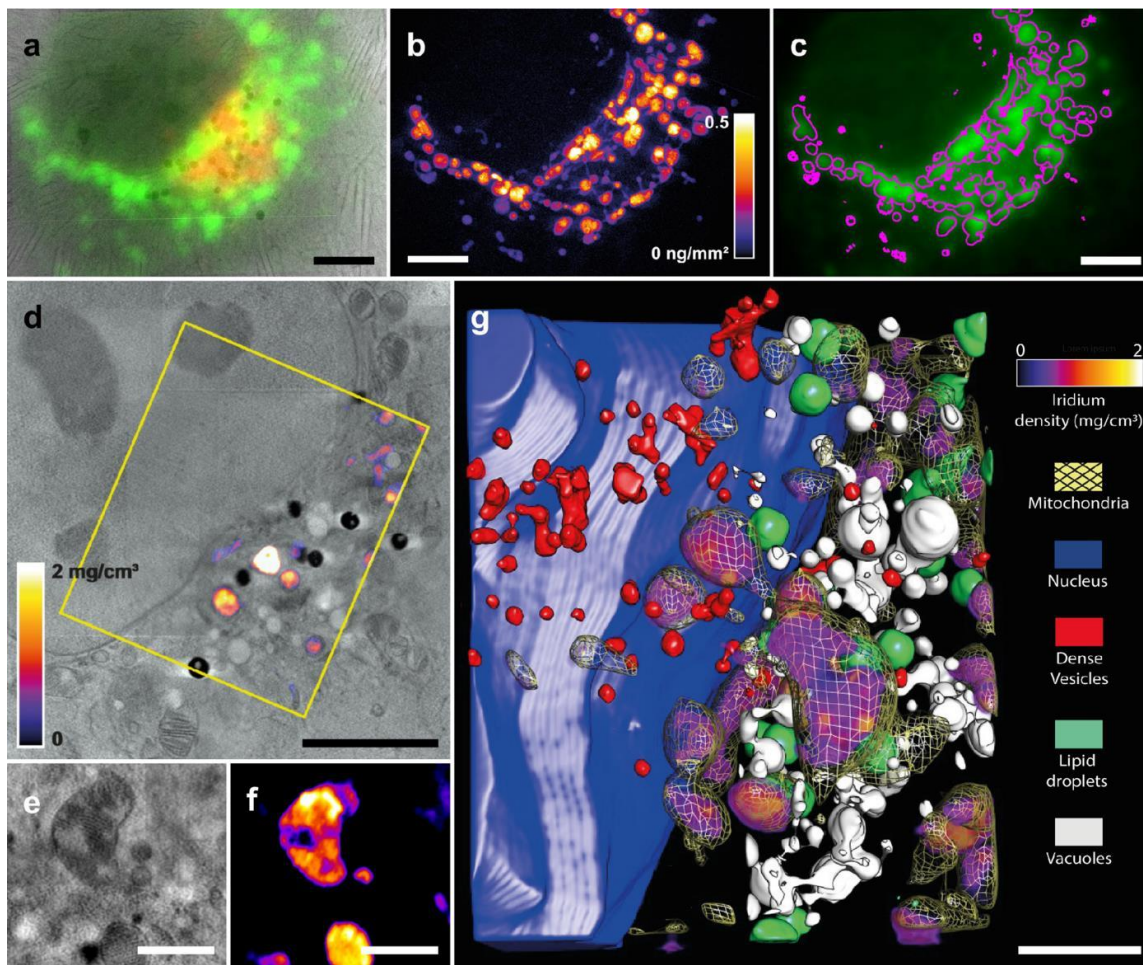
Figure 1. Determination of intracellular location of Ir in breast cancer cells (MCF7). (a) Image of an MCF7 cell treated with 1 μM ACC25 for 12 h, which is an overlay of soft X-ray microscopic imaging (grey) and epifluorescence signal (green, mitochondria; red, acidic organelles). (b) Ir distribution imaged by 2D XRF on the same cell. (c) Overlay of the epifluorescence mitochondria signal (green) with a mask generated using the Ir signal shown in (b) (the two signals are superimposable). (d) Selected area of the cell in (a) shown as an overlap of two reconstructed slices from cryo-SXT and XRF tomography (XRF acquisition area in yellow square where Ir densities are shown). (e) and (f) compare slices of mitochondria from cryo-SXT and XRF tomography results of the same area, illustrating the location and concentration of Ir signal inside mitochondria. (g) 3D rendering of the yellow square area in (d) after segmentation of the organelles. The Ir signal is displayed with the same colour density scale as in (d) and (f), different organelles are displayed. Scale bars: (a)-(d) 5 μm; (e) and (f) 1 μm; (g) 2 μm. From Conesa *et al.*, 2020[31]

Plants also use transition metals to fend-off invading microorganisms. Using different siderophores, plants control the composition of their associated microbiota, limiting the proliferation of pathogens[32, 33]. In addition, plants use nutritional immunity to limit pathogen attack by reducing the availability of essential limiting nutrients such as Fe [34]. Alternatively, metals can also be locally increased to toxic levels in response to pathogen attack[35]. **Cryo-nano-XRF and XANES studies will be critical to understand this aspect of plant immunity at the subcellular level and how to improve it in crops for agricultural activities, particularly considering the emerging plant diseases and the need to ensure food security in the context of climate change. As a result, we will obtain information on how to modulate metal application to combat pathogens, what metal-species/chelators would be more suited for phytosanitary treatments, and which are the traits associated with enhanced metal-dependent immunity to select for.**

Finally, **biofilms** are multicellular microbial communities that encase themselves in an extracellular matrix of secreted biopolymers and attach to surfaces and interfaces[36]. Bacterial biofilms have been intensively studied and recognized as a major bacterial lifestyle in a diverse range of ecosystems. They grow on natural surfaces as diverse as rocks, root plants or teeth, and also develop on synthetic surfaces such as medical devices or water distribution systems. In biofilms, individual bacteria organize themselves in space and time into functionally distinct microenvironments, resulting in phenotypic heterogeneity. Biofilms show remarkable resistance to molecular penetration and eventually lead to high levels of antibiotic tolerance/resistance[37]. In this context, it is crucial to understand the mechanisms that allow this complex matrix to be so robust, identify chemical compounds or agents that can disturb these structures and further, study their mode of action. **More insights into this matter can be achieved by investigating the structural organization of bacteria and intracellular content/distribution of relevant trace elements within native and disturbed biofilms.**

Metal-based nanoparticle drugs and catalysts

Metal nanoparticle (NP)-based drugs are normally composed of a metallic core covered by a polymeric shell that stabilizes their colloidal nature. At the target site, NPs need to be internalized by cells to be released into the cytosol or reach specific organelles to release the therapeutic payload. However, they are not stable assemblies, and after administration may undergo changes in composition, which can reduce their efficacy and be dangerous for cytotoxicity. For example, NP surfaces may be overcoated by a protein corona[38] or suffer enzymatic degradation [39]. Equally, metal cores of NPs can undergo chemical and physical changes once internalized by cells, which could alter their therapeutic activity or cause NP-induced toxicity[40, 41] (*e.g.,* release of toxic metal ions). Thus, to understand the effects of NP-drugs, biological responses need to be correlated with the intracellular location, speciation, and behavior of their components (*i.e.,* metal cores, polymeric shells and any therapeutic units attached to them).

X-ray imaging methods can provide element-specific and precise distribution information of inorganic NPs at subcellular and organelle levels, as well as the morphological information of biological specimens without functionalization or labeling. For example, nano-XRF maps have enabled observation of cellular internalization and degradation of labile Ag particles and nanowires[40-42], Au and Ti NPs [43], Pt-based drugs [44], magnetosomes [45] and CuS nanomaterials[46]. The 3D distribution of 20 nm Ag NPs inside human monocytes at different time points was shown with high spatial resolution using hard X-ray TXM with Zernike phase contrast imaging[47]. These images directly demonstrate the cellular accumulation and exclusion processes of Ag NPs in THP-1 cells[47]. The same method has also been applied to visualize the distribution of TiO_2 NPs and nano-MoS_2 in cells[48].

When investigating metal ion and particle distribution in biological samples, XRF imaging with hard X-rays lack sensitivity for detecting lighter elements, which makes it difficult to obtain structural

information on the tissue and cellular material. This problem can be overcome by the correlative acquisition of phase contrast images as proposed at CORUS.

Organometallic catalysts can facilitate a breadth of chemical reactions inside cells[49-53], including many unattainable by natural enzymes[54-57]. This could transform the fields of chemical biology and medicinal chemistry, as hypothetically only small doses of such catalysts are required to transform large numbers of substrate molecules inside cells. Thus, it might be possible to use organometallic catalysts as therapeutic and biotechnological tools by generating different drugs *in situ* with low overall treatment costs[54, 56-58].

Intracellular organometallic catalysts, such as Ru, Ir, Au, Pd or Os complexes, are originally designed to work under non-physiological conditions [54, 57]. Therefore, their activity is not compatible *in cellulo*, showing low turnover numbers [59, 60]. This suggests that intracellular degradation is a problem for these catalysts, probably due to unexpected changes in pH, redox modulation or the action of enzymes. Degradation would not only decrease catalytic efficiency[61] but potentially lead to unwanted toxic effects (limiting the maximum safe dose), especially upon release within cells of metal ions and other components of the catalyst. For these reasons, they have been mostly ignored as clinical or biotechnological agents until now.

Combined XRF and phase-contrast X-ray imaging of cells in cryogenic conditions can study intracellular degradation processes of organometallic complexes to further advance their potential as biological catalysts. Halogen tags can also be used for XRF mapping to assess the in-cell stability of metal complexes, offering design directions for the development of advanced catalysts with improved cellular stability and efficiency. This strategy revealed unstable Os-based catalysts were degraded by thiols in lysosomes[62] and that Os-based prodrug catalysts were stable under physiological conditions [63].

Correlative XRF-XAS acquired using microfocused synchrotron radiation has been used over the years to study metals in whole organisms (*i.e.* Cu in *Drosophila melanogaster*[64], Fe in *Caenorhabditis elegans*[65]), or exogenous metallic systems in cells (*i.e.* toxicity of Cr^{III} dietary supplements [66]). Yet, only a small number of correlative XRF-XAS experiments have been acquired successfully on cells using nanofocused X-rays (see Fig. 2). For example, XRF maps and nano-XANES obtained from cells treated with an Os-based organometallic prodrug showed a dramatic concentration of unexpected Os^{III} species within mitochondria [67]. Additionally, combined soft X-ray cryo-STXM and correlative hard X-ray XRF-XAS indicated that irradiation of a Pt^{IV} photo-active anticancer drug caused extensive cellular damage, but only 20% of the Pt^{IV} complexes were reduced to active Pt^{II} species during the process [68]. More recently, machine learning algorithms were developed to analyze simultaneous XRF and XANES maps acquired from alveolar macrophages treated with Fe-doped carbon NPs, providing maps of Fe species within cells[69].

Although such correlative studies using nanoprobes are common in Material Sciences, they are difficult to transfer to biology due to the low concentrations of the species studied in cells and the structural-chemical sample alterations caused by long irradiation times. The impact of radiation on biological samples critically depends on their environment and sample preparation, but most importantly the resistance against damage rises exponentially with decreasing temperature[70], so much higher radiation doses can be applied at cryogenic temperatures than at room temperature[71]. **Therefore, CORUS will permit the study of metal nanomaterial and catalyst chemical reactivity in cells by enabling acquisition of correlative phase contrast, XRF imaging, and spectral XAS maps under cryogenic conditions.**
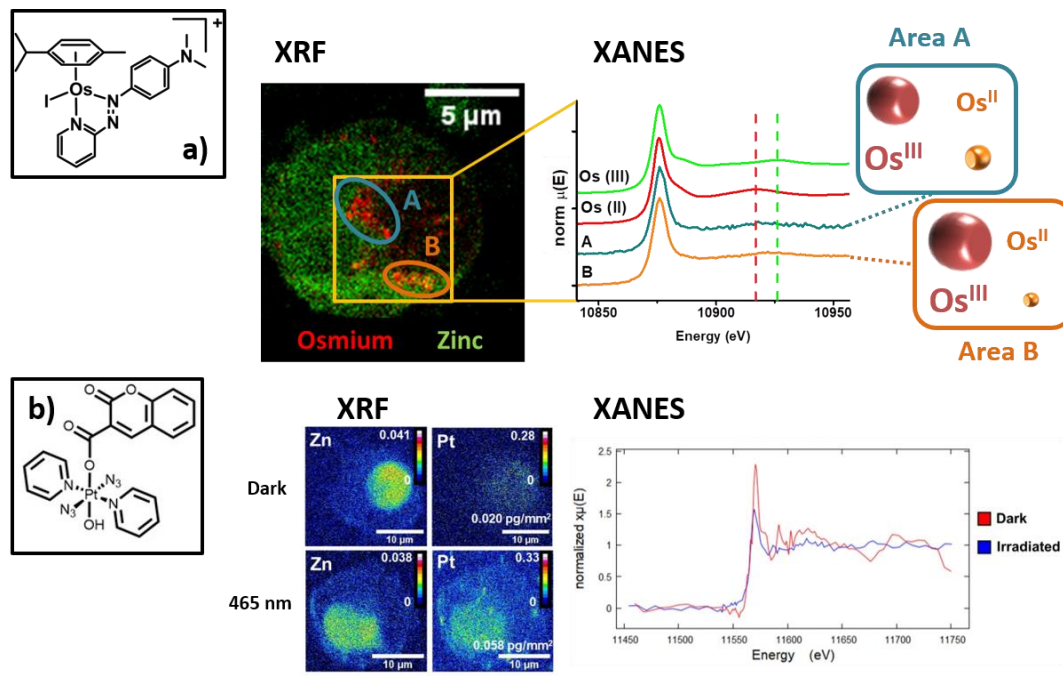
Figure 2. Nano-XANES characterization of metallodrug oxidation state in cancer cells. (a) Os organometallic prodrug [67]: XRF maps show cellular distribution of Os complex and Zn (cell nuclei) in cancer cell. Nano-XANES collected from areas indicated by ellipses (dotted lines show maximum absorbance of secondary peaks from Os^{II} and Os^{III} references). XANES shows that Area A contains 20% Os^{II} and 80% Os^{III}, while Area B contains 5% Os^{II} and 95% Os^{III}. (b) Pt^{IV} photoactivatable[68] prodrug: XRF maps show cellular distribution of Pt complex and Zn (nuclei outline) in cancer cell. Nano-XANES collected in 15x15 μm^2 areas of the cells in the dark (red) and after irradiation (blue). XANES shows a conversion of 27% of Pt^{IV} to Pt^{II} upon irradiation.

Toxicology of metals and micro-/nano-materials

Air pollution is formed by particles of different sizes and chemical composition that cause a range of negative physiological effects, from acute lung toxicity to longer term health issues[72]. Particles below 100 nm ($PM_{0.1}$) are more dangerous as they possess a higher surface to volume ratio and are more reactive [73]. NPs are also more difficult to remove from lungs than larger particles, and once inhaled, can penetrate deep into the alveolar region[74], further entering the circulatory system [75]. In urban areas, NPs are produced mostly by fuel combustion and industrial sources, and contain mostly soot and particles of organic origin [76], but also high quantities of trace metals[77]. Furthermore, substantial amounts of engineered nanomaterials can reach the atmosphere due to the commercial and industrial progress with nanotechnologies. As such, NPs of reactive metals (i.e. Ag, Pd, Pt) can be found in the $PM_{0.1}$ fraction[78] and are responsible for acute lung responses and chronic diseases[79]. Therefore, investigating the biological interactions of metal constituents originating from the $PM_{0.1}$ fraction is crucial to understand the adverse health effects caused by air pollution.

The toxicity of metals found within $PM_{0.1}$ has been studied *in vitro* by exposing lung-derived cells (*i.e.*, macrophages or alveolar epithelium cells) to synthetic metal NP models [80-83] . Remarkably, NPs from both toxic metals (*i.e.* CdO, Co[84])and essential trace elements (*i.e.* Ni, Cu, and Fe[82-84]) cause unwanted cellular effects such as ROS generation, DNA damage, metabolic alterations, and/or dysfunction of vital cellular mechanisms[85]. This could be explained by alterations on the cellular homeostasis, among other cellular effects (*i.e.* redox processes or carcinogenic effects[84, 86]). Similarly, model NPs of soluble metals or metal oxides (*i.e.* ZnO, CuO, or Ag) showed that the toxic effects observed in cells were due to the presence of

9

active free metal ions[87, 88]. These ions could be liberated outside cells and enter through diffusion (*i.e.* ZnO nanoparticles) or in lysosomes due to low pH or peroxidation (*i.e.* AgO or CuO nanoparticles). The latter is known as the "Trojan horse effect"[89] [87], and explains differences in toxicity observed between free metal ions and their NP form[87, 88].

Exposure to asbestos has been a long-standing issue for the health of human populations. Low levels of asbestos fibers are present in soil, water, and air. Generally, exposure to naturally occurring asbestos is minimal and does not pose a health risk. However, if asbestos-containing materials deteriorate or are not properly contained during demolition or renovation, asbestos fibers can be released and become airborne. The fibers can be inhaled into the lungs and remain there for a long time, thus exposing humans to serious health risks. Studies link the inhalation of asbestos fibers to an increased risk of fatal diseases, such as asbestosis, mesothelioma and lung cancer. Even though the link between exposure to asbestos and malignant mesothelioma was demonstrated between the 1950s and the 1970s, little advancements were made in medical treatments, and still today only one in twenty persons are alive five years after malignant mesothelioma diagnosis.

In the lungs, alveolar macrophages have the role of removing foreign particles, and are able to do it efficiently when dealing with common micron-sized particulate matter. However, due to the limited size of macrophages (10 – 15 µm in humans), they are unable to completely engulf high aspect ratio materials with lengths of above ~10 µm and widths of below ~0.5 µm, so as to remove them from the host organism[90]. The resulting frustrated phagocytosis initiates a biomineralization process that deposits organic and inorganic material around the foreign object, forming peculiar structures (named Asbestos Bodies) consisting of an Fe-rich envelope surrounding the original fibers. Due to their dimensions, nanoprobe techniques with high sensitivity (few ppm) and sub-micron spatial resolution are required to study these structures in the lung. Furthermore, most of the studies today[91-93] employed considerable sample manipulation, leaving the open question "if, and to what extent, such methods could alter the chemical and structural properties of the Asbestos Bodies before measurement?". A recent study[94] conducted at the ESRF provided new insights by combining two techniques, scanning X-ray fluorescence spectroscopy and X-ray phase-contrast holo-tomography, to study unaltered lung tissue samples with chrysotile and crocidolite asbestos from former asbestos workers. It was found that asbestos particles develop an Fe-rich coating that becomes the actual interface between the foreign fibers and the host organism. **More investigations are required in order to characterize the origin and formation of the Fe content in asbestos bodies. CORUS can help decipher the effect of toxic micro- or nano-material from pollutants in cells and tissues, underlying the chemical processes involved and understanding the origin of related diseases.**

Tissues and imaging

In complex multicellular organisms, such as humans, cells are organized into tissues. Tissues refer to clusters of comparable cells that execute a common function. At each level of organization, from cells to organ systems, structure and function are intertwined. Each type of tissue is susceptible to a variety of diseases. Understanding the mechanisms at different scales is crucial for developing effective treatments and preventative strategies to improve human health.

X-ray phase-contrast imaging techniques have proven to be valuable tools for providing enhanced sensitivity at a reduced radiation dose. These techniques are particularly important for radiation-sensitive and low Z samples, such as biological ones. The use of propagation-based phase-contrast imaging, including its prominent application holotomography, has gained widespread recognition for its ability to provide high-resolution quantitative imaging[95]. This technique combines the principles of holography and tomographic reconstruction to obtain information about the real and imaginary components of the

refractive index. With in-line holography, a partially coherent beam interferes with itself, thereby eliminating the need for a separate reference beam. Holotomography has been demonstrated to provide exceptional results in nano-computed tomography (nano-CT) applied to different areas, including neuroimaging [96-98], studying bone and cartilage[99, 100 3], and understanding cardiovascular changes and injuries associated with aging and/or genetic alterations[101].

Neuroimaging & connectomics: In medical research, visualization plays a crucial role since abnormalities in the size, shape, or topology of neurons and brain disorders have a direct correlation with each other. Many pathological brain conditions are linked with cell loss, abnormal cellular morphology, and dendritic morphology. Furthermore, neurodegenerative disorders are characterized by changes at the subcellular level, including membrane damage inducing curvature adaptation, axon demyelination, and abnormal morphology of microglia in Alzheimer's disease. Finally, cognitive functions are ultimately encoded by the flow and processing of information across neuronal circuits, from sensation to the generation of motor outputs. Therefore, advances in the mechanistic understanding and treatments for diseases characterized by the alteration of cognitive functions can come from a better understanding of the function and structure of neuronal circuits. However, neuronal circuits are challenging to study: their dimensions span across > 6 orders of magnitude, from 1 mm^3 (the volume that contains the input & output neurons and their connectivity for the smallest mammalian neuronal circuits) to few nm (membranes and synapses). Barbone *et al.*[102] demonstrated how the application of X-ray multiscale 3D neuroimaging allows to investigate cellular aging and neurodegeneration in Alzheimer's disease models postmortem. This technology allows researchers to study the three-dimensional structure of the brain at high resolution, enabling the quantification of morphological changes in neurons and their subcellular structures over time. Using this approach, researchers can gain insights into the cellular mechanisms underlying neurodegenerative diseases such as Alzheimer's disease, potentially leading to the development of new diagnostic tools and therapies. At the synaptic level, a "complete" and "dense" wiring diagram of a neuronal circuit - its connectome - provides essential knowledge to model and predict how it processes information[103, 104]. However, density and completeness impose two requirements: one on detail, being able to resolve all synapses and to trace all neuronal wires (dendrites and axons); and one on volume, being able to map a landscape that contains the entire circuit under study. To satisfy the latter, volumes in the range of (0.2 - 1 mm)^3 can be sufficient to contain individual targeted neuronal circuits or brains of small animals[105], whereas a whole mouse brain would require 500 mm^3 [106]. To satisfy the former, resolution must be sufficient to delineate plasma membranes and synaptic junctions, requiring a granularity of (10-40 nm)^3 [107]. Moreover, a mechanistic understanding of how neuronal circuits process information cannot always be derived from studying their structure or their physiological function in isolation. Instead, studies that integrate both data streams hold much more potential to uncover the computational logic employed[108]. As demonstrated by Bosch *et al.* [109], the integration of multiple imaging techniques such as *in vivo* physiology, synchrotron sub-microtomography, and volume electron microscopy allows for functional and multiscale 3D structural investigation of brain tissue (**see Fig. 3**). This approach provides unprecedented insights into the complex architecture of neural circuits, enabling the mapping of neuronal connectivity and the investigation of functional dynamics at the cellular and subcellular levels. Furthermore, the correlative application of these techniques can help bridge the gap between structural and functional neurobiology, providing a comprehensive understanding of the brain's complex network of cells and their interactions. This has implications for the development of new treatments and therapies for neurological disorders that involve alterations in neural connectivity and function.
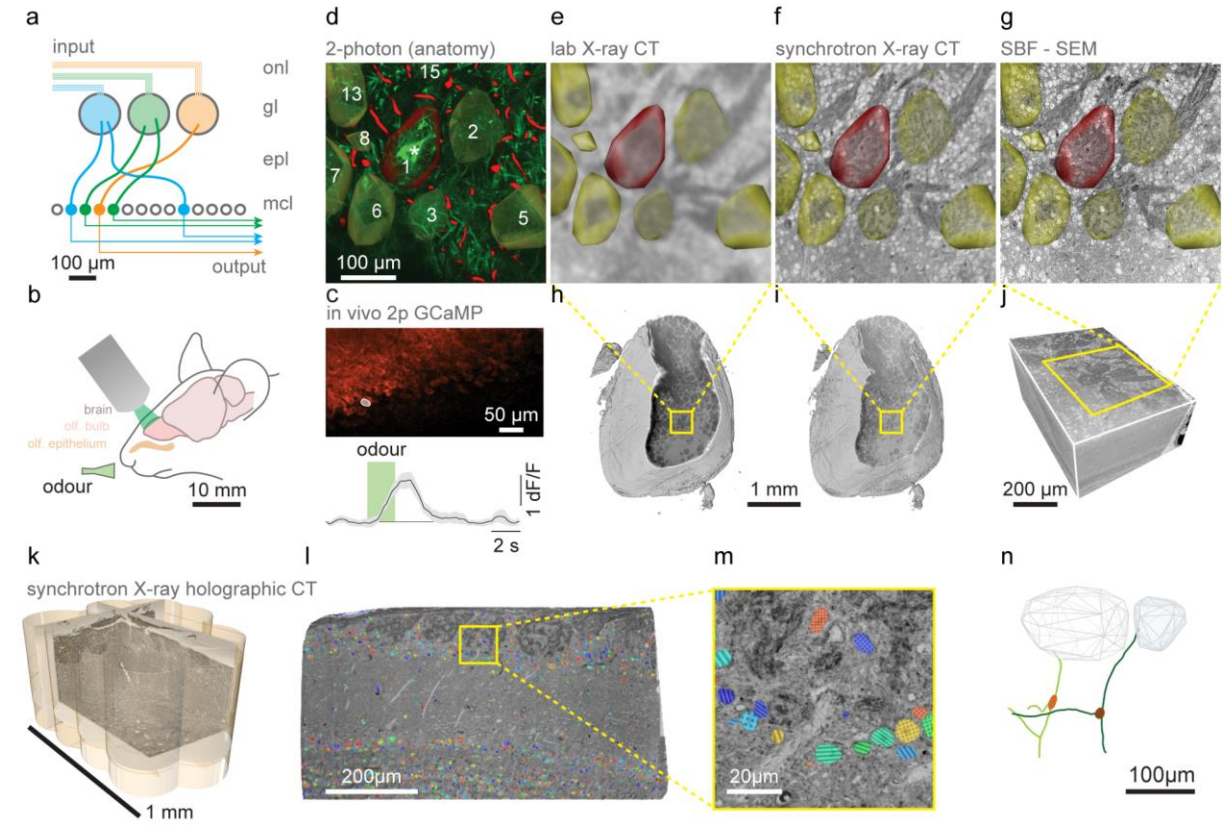
Figure 3. Study of function-structure signatures of mammalian neuronal circuits using correlative 2-photon, synchrotron X-ray and volume electron microscopy. (a-c) Mammalian neuronal circuits can be found embedded in 1 mm³ volumes and can be interrogated using *in vivo* 2-photon microscopy (b). (c-g) A correlative multimodal imaging pipeline allows retrieving the function (c) and structure of the same neuronal circuit, by mapping the same sample at different length scales and detail. X-ray (e-f) and volume electron microscopy (EM) techniques (g) (in this case, serial block-face scanning EM) are compatible. X-ray imaging techniques can provide insights on the structure of the sample non-destructively, de-risking the workflow significantly as well as improving its reliability. Furthermore, synchrotron X-ray CT provides sub-cellular detail (f) across multi-mm³ tissue volumes (i), a volume larger than the one at reach by SBF-SEM (j). (k) X-ray holographic nanotomography (XHN) provides sub-μm detail across near mm³ volumes non-destructively through tiled acquisitions later stitched into a continuous dataset. XNH is compatible with the previous workflow. (l-m) Subcellular features of interest such as cell nuclei (m), can be segmented automatically across the whole dataset (l). (n) Neuronal morphologies and circuit structures can be extracted from such datasets. (a-j) adapted from Bosch *et al.*, 2022 [109]. (k-n) preliminary results from the Schaefer Lab (The Francis Crick Institute, London, UK), manuscript in preparation. (f) was acquired at Diamond I13-2. (k-m) was acquired at ID16A, ESRF.

Altogether, the multi-scale and multi-modal study of biological soft tissues such as the brain is a nascent and growing research field that will benefit from beamlines mapping mm³ volumes at subcellular resolution, both alone and in combination with other imaging modalities using light and/or volume electron microscopy.

Bone imaging: Bone is an extraordinary natural material that possesses the unique combination of strength and lightness, attributed to its hierarchical structure and composition at various length scales. Despite its strength and resilience, bone is a dynamic tissue that has the ability to sense and repair damage caused by external mechanical stress. However, the precise mechanisms that govern these processes are not fully understood, mainly due to the intricate 3D organization and the interplay of mechanical and biochemical factors at the cellular level. The lacunocanalicular network (LCN) is a complex interconnected porous system embedded within the mineralized bone matrix at the cellular scale. Osteocytes, the most

abundant bone cells, are located within the lacunae and play an essential role in bone remodeling. Osteocytes act as regulators by producing WNT1 to control bone formation and activating NF-κB ligand (RANKL) to recruit osteoclasts. The LCN facilitates communication and nutrient transport between osteocytes via the canaliculi that connect the lacunae. Osteocytes sense local loading and interstitial fluid flow in the bone matrix, producing and exchanging stimuli signals to regulate bone cell activities.

Disorders of bone fragility often arise from an imbalance in the bone remodeling process, which involves the resorption and formation of bone tissue. Osteoporosis is a bone disease characterized by a reduction in bone mass and density, which can lead to fractures even from minor injuries. It is a significant social and economic problem, with millions of people affected and billions of euros in costs. Understanding the 3D structure of cortical bone is essential to comprehend bone mechanical properties and fragility. At the cellular scale, the LCN plays a crucial role in bone remodeling and maintenance, allowing for communication and nutrient transport between osteocytes. **In recent studies, 3D X-ray nano-CT has proven to be a suitable technique for imaging the bone LCN and for the quantification of the LCN architecture, which is required to understand its role in bone strength and maintenance[100, 110, 111].**

Biomineralization

Biomineralization is the formation of a condensed mineral/crystal phase often associated with biomass or organic matrix material. It is an extremely widespread phenomenon, found in all six taxonomic kingdoms. Thus, biomineralization occurs in a number of living systems, from coastal ecosystems (calcium carbonate in corals), to the human body (calcium hydroxyapatites bones and teeth), to even within individual bacteria (iron oxides nanocrystals [112]). Understanding mechanisms for biomineral formation at the nanoscale can lead to improvements in regenerative healthcare technologies (e.g., remineralization of bone, teeth and tissue[113]) and further adapt biologically-controlled mineral formation to sustainably produce robust and high performance materials [114]. Moreover, there are still unresolved biomineralization processes in the human body such as the biosynthesis of magnetite in the brain and other cells that need to be addressed[115].

Bone biomineralization: Hydroxyapatite (HA) is a naturally occurring mineral form of calcium apatite, bearing substituting metals such as Zn, Mg and Sr, found in many tissues including bones[116] and cartilage[117]. Biomineralization is a lifelong process, fundamental in bone formation, repair, and remodeling. Biomineralization of bone depends on the complex crosstalk between osteoclasts, osteoblasts, and osteocytes. Osteoclasts digest bone matrix while osteoblasts synthesize it and orchestrate its mineralization[118]. Osteoblasts are derived from bone mesenchymal stem cells (bMSCs), and once they are trapped within the bone they have formed, they terminally differentiate into osteocytes. Osteocytes are interconnected stellar cells, which integrate mechanical and biochemical cues that govern bone deposition and resorption.

As the precursor of osteoblasts and osteocytes, bMSCs are heavily investigated to unveil the molecular basis of osteogenesis, to translate basic knowledge to application in tissue engineering and regenerative medicine. In particular, human osteosarcoma (OS) could benefit from this research field, since defective osteogenesis and biomineralization are typical features of this pathology. OS is a malignant sarcoma characterized by the formation of immature bone, which is associated with a poor prognosis due to the high incidence of metastasis and frequent chemoresistance[119]. Despite efforts made by clinicians in the last 30 years, the 5-year survival rate of high-grade OS is limited to 70%, hence the development of innovative and more selective strategies to improve the survival of OS patients is a compelling unmet need[120]. The use of X-ray synchrotron-based nano-techniques to study at cellular level allows to i) check and track which alterations occur in the genesis and evolution of intracellular and extracellular mineral

depositions in OS; ii) provide a deeper comprehension of the bone mineralization process in OS cell and iii) improve the chance to translate the new knowledge in OS clinical practice and treatment.

Calcium is a crucial element for bone formation and is present in the extracellular mineralized matrix as an integral component of hydroxyapatite crystals[121]. Very little is known about the intracellular Ca concentration, distribution, and homeostasis in bMSCs, and even less about the progression of the extracellular Ca-phosphate and -polyphosphate deposition during osteoblast differentiation. In fact, this core knowledge is provided by studies on the advanced phases of biomineralization, which mainly occur in the extracellular matrix, while studies on the early stages of this process are scarce. This gap could be overcome by the combination of X-ray microscopy-based techniques and cryogenic conditions to be implemented at the CORUS beamline, allowing the biomineralization phenomenon within the intracellular matrix and organelles to be followed. Recently, Procopio *et al.*[122] provide a quantitative assessment of mineral deposition chemical composition together with their molecular and crystalline structure characterization within differentiated bMSCs combining soft X-ray tomography and spectro-microscopy, as well as XRF.

Studies on bMSCs differentiated towards osteoblasts[123] suggest crystalline calcite is a precursor of hydroxyapatite depositions within the cells during biomineralization. In particular, both calcite and hydroxyapatite were detected within the cell during the early phase of osteogenic differentiation. This striking finding may redefine most of the biomineralization models published so far, taking into account that they have been formulated using murine samples while studies in human cell lines are still limited.

The combined nanoscale imaging and spectroscopy capabilities of CORUS would be able to further probe cryo-preserved biomineralizing human cells; investigating the morphology, the elemental composition and the chemical properties of precursors at varied stages of biomineralization. Uniting imaging of relevant elements in human osteogenesis (e.g., Ca, P, Zn and Sr) and their spectroscopic analysis (Ca K-edge XANES) will help unveil key cellular mechanisms during bone biomineralization.

Microbial biomineralization: The steady increase of CO_2 concentration in Earth's atmosphere and its resulting effect on climate change is heavily researched across scientific disciplines and on different scales. More than 25% of CO_2 produced by human activity is absorbed into our oceans, which lowers the pH (ocean acidification) and causes potential problems in the cell physiology of marine life, particularly shell-building organisms. Though small in size, the abundance and biomineralization activities of calcifying organisms (e.g., mollusks, foraminifera) and phytoplankton (e.g., coccolithophore microalgae) play a significant role in regulating local chemistry of marine ecosystems with some influencing the carbon cycle by sequestering and depositing carbon onto the ocean floor, acting as carbon sinks (e.g., coccolith sedimentation)[124]. Researchers are currently trying to anticipate the effect of CO_2 increase and other climate change-related issues (e.g., ocean acidification, average ocean pH drop from 8.2 to 7.8 by 2100) by monitoring biomineral production in the environment and under laboratory culture conditions. However, our fundamental understanding and ability to predict the effect of our future oceans and environment is blocked by our still-developing view of biomineralization mechanisms[125].

Coccolithophore microalgae are miniscule calcifying organisms, intracellularly producing nanocrystalline calcitic biominerals, known as coccoliths, that are excreted to the cell surface. Impressively, coccoliths produced by coccolithophores account for almost half of the oceanic carbonate deposits[126]. This biomineralization activity has a gigantic impact on Earth's geology (sedimentation and snow ballasting) and marine ecological systems (bloom generation augments local availability of nutrients for marine microorganisms). Towards an understanding of coccolith formation in the most prominent coccolithophore species, *Emiliania huxleyi*, studies employing cryo X-ray microscopy and nano spectroscopy have revealed a previously unknown intracellular body that may play a role in storing or shuttling Ca-based precursors (disordered calcium and phosphate materials) for coccolith formation[127].

Further studies confirmed the role of this intracellular body for Ca-P storage with X-ray absorption spectroscopy to follow Sr speciation during coccolith formation[128]. More recent results further revealed the delivery of precursors to the site of biomineralization in greater detail, capturing high resolution snapshots of coccolith formation [129]. The intracellular dynamics and strict control over mineral formation by coccolithophores demonstrates a complex process yet to be elucidated. **The combined nanoscale imaging and spectroscopy capabilities of CORUS would be able to further probe vitrified biomineralizing microalgae to investigate the elemental composition and chemical properties of precursors and at varied stages of formation. In particular, near-native state spectroscopic analysis (Ca K-edge XAS) will help decipher key chemical mechanisms during CaCO$_3$ formation. To the best of our knowledge, there is currently no nanoprobe end-station in Europe that offers sub-100 nm beam sizes, cryogenic conditions and Ca K-edge XAS. This will open new opportunities at nanoSpec of CORUS to reveal the local structure of forming CaCO$_3$ in a number of biological conditions.**

Only in recent years have prokaryotes such as cyanobacteria and magnetotactic bacteria been shown to biomineralize intracellular CaCO$_3$ in the form of amorphous calcium carbonate (ACC) nanoparticles or granules[130, 131]. Along with other microalgal biomineralizers, the impact of these newly discovered intracellular CaCO$_3$ producers on our environment is to be further understood[132]. **The given size of ACC inclusions, their density and their inherent metastability would be perfectly suited for investigation with the proposed beamline setup with CORUS (i.e., hard X-ray energies, vitrified samples, Ca, P, Sr, Ba XRF, and Ca/Sr/Ba XANES).**
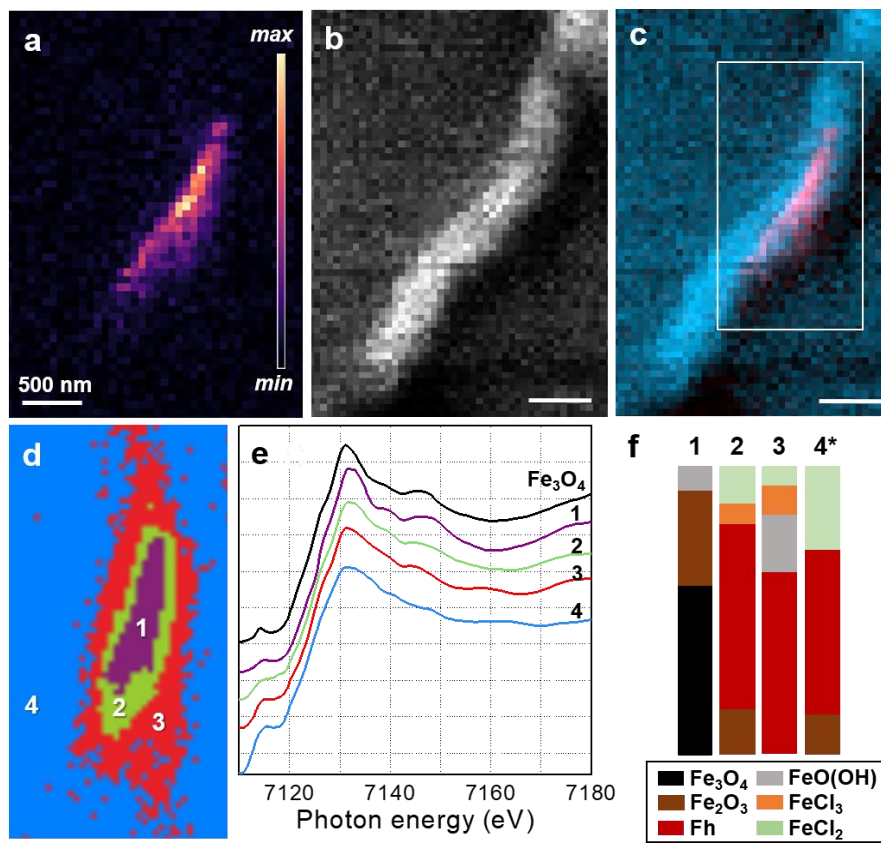
Figure 4. Nano-XANES characterization of magnetite (Fe$_3$O$_4$) nanocrystals within a bacterium. (a) Fe Kα XRF map of a magnetotactic bacterium with an intracellular chain of Fe$_3$O$_4$ nanocrystals and intracellular Fe species. (b) X-ray phase-gradient normalized map. (c) Combined Fe Kα XRF and phase-gradient maps. (d) Cluster analysis of Fe K-edge XANES stack collected for the rectangular region in panel c. (e) Corresponding Fe K-edge XANES spectra (with Fe$_3$O$_4$ reference) for four definitive cluster regions that represent Fe chemical species around Fe$_3$O$_4$ nanocrystals. (f) Linear combination fitting results of Fe K-edge spectra for each of the four cluster regions with representative Fe-based reference materials (Fh - ferrihydrite). Adapted from Chevrier et al. Small Sci. 2022, 2, 2100089.

Bioremediation, food security and sustainable agriculture

Though small in size, microorganisms are capable of sequestering or precipitating a relatively large quantity of metals from aquatic environments. Harnessing these biomineralization pathways is a potential biotechnological strategy to depollute contaminated water systems and/or to recover precious metals from water or soil[133-135]. Understanding this biomineralization activity or metal-uptake mechanism will help optimize their performance for application in the field. Towards this end, the combination of sub-100 nm beam size and hard X-ray energies has recently given X-ray nanoprobe techniques the possibility to reveal chemical and physical phenomena on the subcellular level[136, 137] (**see Fig. 4**).

Heavy metal contamination is one of the major abiotic stresses that cause environmental pollution. Although heavy metals are naturally occurring in the soil, geologic and anthropogenic activities increase their concentration up to a harmful level for both plants and soils because of potential toxicity, which disturbs their physiology and development. These metals or metalloids are taken up by plant roots and translocated to the shoot system and further pose a potential threat to human health as they enter the food chain. Among the techniques used for soil remediation, phytoremediation is a suitable strategy based on the use of vegetation and rhizosphere microorganisms to remove pollutants. Phytoremediation strategy requires the use of tolerant plants that can extract contaminants to their aerial part (phytoextraction) or accumulate them in the root system (phytostabilization). Understanding the mechanisms by which plants take up and detoxify metals is one key factor to increase the efficiency of this technology.

The increasing number of patents that use NPs in agriculture suggests that the application of nanomaterials will continue to grow (nano-agrochemicals). Though properties associated with nanosized objects might be desirable, they can pose a threat to the environment since their fate is poorly understood. Silver NPs, for example, are now used in commercial products for diverse applications, mainly due to their antimicrobial properties. They are used in textiles, food preservation, cosmetics, drug delivery, and agricultural inputs. Several authors have shown that these nanomaterials can accumulate in plants and induce toxic effects[138-142]. **Understanding the translocation to edible vegetables, the interaction mechanisms between pollutants and the different organs of plants, the change of speciation within the plant and possible detoxification mechanisms as well as the impact on the plant ionome is of utmost importance.** In addition to conventional scanning electron microscopy and Fourier transform infrared spectroscopy, **cryo X-ray spectromicroscopy techniques with nanoscale resolution are becoming essential to accomplish the task**.

Transition metals play a critical role in plant growth, productivity and nutritional value. Low metal bioavailability in many of the main agricultural areas of the world lead to reduced crop yields and to Fe and Zn deficiency in the diet, which are two of the three main causes of malnutrition in the world[143, 144]. Studying elemental distribution and speciation in plants has led to the identification of critical metal transporters and siderophores that have subsequently been used for nutrient bio-fortification strategies[145]. Additionally, understanding and visualizing metal selectivity would lead to reduced accumulation of toxic elements (such as Cd or Hg). Metal deficiency in crops is typically treated by metal fertilization. However, it is still poorly understood how these fertilizers are used by plants, how they are introduced, and the preferred chemical forms of the metal. **XRF and XANES will be essential towards improving metal fertilizer design and application**. Moreover, metal transfer is used by plants to select for beneficial plant-associated microorganisms. This is particularly important in the case of diazotrophic microorganisms that, by fixing N_2 in NH_3, reduce the need for expensive and polluting synthetic nitrogen fertilizers of modern agriculture[146]. One of the best examples is the partnership between legumes and rhizobia in root nodules, a keystone of crop rotation strategies, in which **XRF and XANES studies are**

beginning to show how metals are exchanged between symbionts and how nitrogen fixation is affected by it[147].

Description of the technologies and methodologies enabled by the beamline.

CORUS end-stations will house two X-ray nanoscopes with built-in cryogenic capabilities. Sample preparation is one of the most fundamental steps and should aim to preserve the structure and chemical composition of cells as close as possible to their native state. Hence, cryogenic capabilities (100 K) will prevent artifacts associated with the chemical fixation and dehydration process of biological samples.

NanoImag end-station will facilitate two main programs: 3D cryo-nano fluorescence (XRF) and 3D cryo or room temperature (RT) phase contrast imaging (PCI) based on the propagation-based technique. The cryo-nano XRF program will enable 2D and 3D imaging and quantification of trace endo- and exogenous elements at very high sensitivity (parts per million level) in whole prokaryotic and eukaryotic cells in near-to-native conditions or tissue sections. The cryo/RT PCI program will reveal the ultrastructure of isolated cells, organoids, or biological soft tissues with a focus on tomography stitching for imaging large volumes up to 0.5 mm in thickness when densely stained with heavy metals, and extending to mm^3 volumes when employing lighter staining methods. Correlating the two imaging modalities will provide chemical elemental imaging in the context of the cellular ultrastructure.

The spatial stability of this end-station at 100 K and the high flux at the nanofocus ($>10^{11}$ ph/s) represent the main figures of merit to reach the needed sensitivity for trace elements and increase data throughput. To improve beamtime efficiency, multiple sample loading into the cryo microscope vacuum chamber will be designed to minimize sample exchange time and allow user autonomy. To establish NanoImag's uniqueness and efficacy, three fixed energies will be used: 10 keV, 19 keV, and 27 keV. Cryo nano-XRF at 10 keV will maximize fluorescence from first-row transition metals, while higher energies (19 keV & 27 keV) are required to reach second-row transition-metals such as Ru, Rh, Ag, and Cd. Cryo or RT PCI will be optimized at 19 keV in terms of hardware performance and will allow for a relatively large field of view. To image highly absorbent, stained, and thick tissue samples, a 27 keV beam is essential. Stitching tomograms will permit imaging large volumes such as those needed when dealing with biopsies or neuronal circuits. The choice of 10 keV makes the beamline optimal for detecting many relevant biological elements and metals (*e.g.,* P, S, K, Ca, Mn, Fe, Co, Cu, and Zn) in biological systems with very high sensitivity.

NanoSpec will be one of the few beamlines in Europe (together with the ID21 nanoscope with 100 nm focus which will be operational in 2024 at the ESRF) to allow cryo spectromicroscopy (2D/3D XRF maps varying the E and single point nano-XANES spectra), though it will be the only one with 3D capabilities. The cryogenic capabilities are essential for probing chemical states at the cellular level in close-to-native conditions and will enable understanding the mode of action of drugs and their toxicity, biomineralization and bioremediation processes, among others.

Advantages and benefits in comparison to competing tools and techniques

CORUS will be unique in the European landscape when considering the following points: 1) the energy choice of 10 keV for **NanoImag** is specifically optimized for 2D and 3D cryo-nano-XRF of oligoelements with a focal spot of about 20 nm and very high sensitivity; 2) spectromicroscopy in fluorescence or absorption modes will be performed with a focus of 30-50 nm in cryo conditions both in 2D and 3D; 3) **NanoImag** and **NanoSpec** will allow direct sample transfer and therefore the end-stations will be complementary and correlative approaches on the same samples will be enabled.

The goal of CORUS is to link cellular function, structure, elemental distribution and chemical information in close-to-native conditions to better address the societal challenges of the future. Nevertheless, cryo-nano-XRF alone has severe limitations: the cellular ultrastructure cannot be revealed unless specific X-ray fluorescent tags are used (not always available or feasible). Therefore, its combination with phase contrast imaging will enable putting into context the elemental distribution within the cellular ultrastructure when labeling is not possible. Moreover, phase contrast imaging at sub-100 nm resolution opens the door to properly address tissue imaging with convenient field of view and throughput required for scientific relevance (e.g., long range tissue organization) and statistical purposes (*e.g.,* addressing sufficient number of samples for probing disease conditions and inter-individual variability).

Regarding competing instruments in Europe, ID16A-ESRF[148] is dedicated to cryo-nano-XRF and phase contrast imaging at 17 keV and 33.6 keV. The fluorescence yield of oligoelements, however, is not optimal at these energies, and will be better addressed with the CORUS working energy of 10 keV. Additionally, ID21-ESRF[149], is currently building a nanoscope end-station with a 100 nm focus expected to be operational in 2024. This end-station will allow 2D spectromicroscopy at cryo conditions from 2-9 keV. **NanoSpec** will therefore complement and go beyond these capabilities with a smaller focus, a broader energy range (4-27 keV) and unique tomography capabilities. Finally, Max IV is currently building a cryo-nano-XRF end-station for NanoMax[150] (5-28 keV, 60 nm focus with tomography capabilities), but this beamline is multipurpose and not specifically dedicated to biological research.

Currently, there are few existing beamlines providing 3D phase contrast imaging of tissues at sub-100 nm resolution. In particular, there is but one, ID16A-ESRF, that addresses the need of a large field of view (≤1 mm) and it is largely oversubscribed. CORUS will help cover this high demand with an exceptional spatial resolution and high-throughput, as performed at the ESRF: one nano holotomogram is currently acquired in 3 h, while ptycho-tomography requires 15 h or more, a severe limitation. Note that inter-individual variability of human/animal biopsies can only be conveniently addressed with high-throughput techniques capable of resolving tissue volumes of about 1 mm^3. Therefore, X-ray nano holotomography is an important tool to progress towards our understanding of tissue organization[98].

Potential synergies with other already existing programs at ALBA

Correlative microscopy, the combination of capabilities and advantages of different imaging techniques on the same sample, is an indispensable tool for Health and Life Sciences research[151]. Correlative microscopy gives access to information that cannot often be obtained by individual microscopy approaches alone. XRF imaging provides limited information on the cell ultrastructure and consequently, there is a need for the implementation of correlative approaches able to provide the cellular context for the elemental analysis. Correlative approaches between visible light microscopy and electron microscopy (CLEM) are well established[152], but equivalent ones (*i.e*., two X-ray imaging techniques) joining elemental imaging and methods able to provide structural information are less advanced. Nevertheless, some examples have already demonstrated the power of such approaches[153, 154]. For instance, visible light fluorescence microscopy can be performed prior to cryo-fixation and XRF imaging to provide the spatial localization of fluorescently labeled organelles, structures or even molecules[155]. XRF can also be correlated with transmission electron microscopy (TEM) on stained resin embedded thin sections[156, 157]. Note that approaches starting with TEM imply sample fixation (chemically or by cryo-fixation), dehydration, resin embedding and finally sectioning. These sample processing steps are accompanied by artifacts that can lead to misinterpretation. Alternatively, biological samples can be vitrified and analyzed in cryogenic conditions making the sample preparation less laborious, preventing the generation of artifacts and hence obtaining data at close-to-native conditions[31]. All these above-mentioned examples make use of different imaging platforms which means there are risks in transferring samples and the mandatory use of

compatible sample supports. More straightforward strategies would integrate in the same microscope different and complementary imaging methods[158, 159].

The techniques enabled by CORUS would be extremely beneficial for the Life Science research at ALBA-II as they will be synergistic to existing ones and others implemented in the future. Correlative and/or multimodal approaches including CORUS, MISTRAL, MIRAS and FAXTOR beamlines would be advantageous to exploit the maximum possible information of a specific biological system within the same facility. A cryo correlative approach with MISTRAL will allow the 3D overlaying of elemental and ultrastructural information provided by cryo-SXT at similar nanometer resolution [31]. CORUS beamline data could be integrated with information from the cryo 3D Structured Illumination Microscope (SIM) available at ALBA. As a result, functional and localization information of specific cellular compartments or molecules provided by cryo-3D-SIM could be combined with XRF information to produce a more efficient workflow. Cryo-3D-SIM can also be integrated with phase contrast imaging to distinguish, for example, different components of the endocytic compartment, information that cannot be obtained only from the cellular ultrastructure. Data produced at CORUS could further be complemented by information on the redox state of the cell provided by MIRAS[160]. Moreover, data from CORUS could be integrated with future technologies at ALBA, such as cryo electron tomography (cryo-ET), cryo focus ion beam scanning electron microscopy (cryo-FIB-SEM)[161] or cryo plasma-SEM[162]. For example, cryo-ET high resolution information[163] of purified samples (*e.g.*, exosomes), cellular or tissue lamellae (prepared by cryo-FIB/plasma-SEM) could be combined with elemental information and speciation to produce more complete and relevant information. Furthermore, cryo-FIB/plasma-SEM volume imaging[162] could be used to provide ultrastructural context to CORUS information.

Another important synergistic aspect is the availability of equipment and expertise for sample preparation already at ALBA. Cryogenic sample preservation requires specialized equipment that allows the generation of vitreous biological samples. This technology is already at hand at MISTRAL. Also, additional sample preparation technologies such as high pressure freezing (HPF) for thick sample vitrification (tissue or thick cells) could be used at CORUS. This technology could also be coupled to visible light microscopy, electrostimulation or optogenetics to gain temporal resolution information[164].

Correlative synchrotron tomography with propagation-based phase-contrast and holotomography studies, which would involve imaging the same specimen at FAXTOR and then at CORUS, will provide targeted subcellular detail across a mm^3 volume within the context of specimens spanning multiple mm^3, meeting the landscape requirements for connectomics studies, among others, and approaching the resolution needed, all the while remaining compatible with follow-up targeted volume-EM approaches. Furthermore, these studies will be compatible with prior visible light microscopy approaches of the same specimen, and therefore be able to resolve structure-function relationships in biological soft tissues. This will prove to be of outstanding interest for the neuroscience field, but also for other fields in biology such as those characterizing tumor microenvironments, immunological tissue systems or in plant science.

Last but not least, CORUS is at the heart of the ongoing project REACH-OneHealth, a new center aiming at societal bio-preparedness, that is, the effective mitigation of the imminent and long-term threats for health, food and environment security arising from climate and societal changes. The center will respond to the multiple challenges raised by One Health, as defined by the World Organisation for Animal Health (WOAH). The center foresees the use of the two end stations of CORUS, plus a replica of the nanoImag end-station in an environment with biosafety level 3.

Potential impact of the instrument on larger national initiatives

As previously noted, sample preparation is a fundamental step for achieving reliable and scientifically relevant data and the gold standard is vitrification, the method of choice at CORUS. This sample

preservation method is, still nowadays, not accessible in all laboratories. ALBA, through JEMCA and MISTRAL, has the needed instrumentation but it is not always feasible nor practical to perform all the required steps prior to vitrification at the synchrotron. Therefore, other facilities, such as advanced cryo-electron microscopy infrastructures (at CNB-CSIC in Madrid or Instituto de Biofísica in Bilbao), technical services at several universities (e.g., UAB, Barcelona) and research institutes (e.g., IRB, Barcelona) can provide access to this instrumentation and expertise for potential national and international users, avoiding the saturation of ALBA facilities. Additionally, the presence of cryo-FIB-SEM equipment at advanced facilities could further strengthen the synergies with CORUS. The phase contrast imaging program could also benefit from the sample collections currently available at pathological anatomy tissue banks such as the Biobanc - Banc de Teixits Neurològics at Parc Sanitari Sant Joan de Déu (Barcelona); the Biobanc at Hospital Clínic (Barcelona) and the broader Instituto de Salud Carlos III (ISCIII) platform of Biobanks and Biomodels (Madrid), among others.

Another national initiative that could benefit from the use of CORUS would be the Distributed Biomedical Imaging Network (ReDIB), which includes biomaGUNE (San Sebastian), CNIC (Madrid), La Fe Sanitary Research Institute (Valencia) and Complutense Bioimaging Center (Madrid). The network aims at providing access to various biomedical imaging technologies such as magnetic resonance imaging, computed tomography and positron emission tomography, among others. ReDIB also promotes collaboration and knowledge sharing among imaging experts and the broader scientific community. In this context, CORUS could interact with the ReDIB network to benefit from access to a wider network of researchers, clinicians and industrial professionals. Analogously, CIBER (Centro de Investigación Biomédicas en Red) is a network of national biomedical research centers that operates under the auspices of the ISCIII. The CIBER program is designed to promote interactions among researchers and institutions working in different fields of biomedicine including bioengineering, biomaterials, nanomedicine, cardiovascular diseases, cancer, neurodegenerative diseases, rare diseases, epidemiology and public health. By collaborating with CIBER, CORUS could have access to a wide range of expertise and knowledge in these areas, which could help to identify new applications for the beamline in biomedical research. In addition, CIBER promotes collaboration among researchers and institutions working in different fields of biomedicine, which could help foster new collaborations and partnerships.

Another fundamental and demanding step for CORUS would be the data processing. Infrastructures such as the Barcelona Supercomputing Center (Barcelona) or DIPC-supercomputing Center (San Sebastian, which has dedicated nodes for image analysis) for big data processing (phase contrast imaging volumes) could potentially be interested in collaborations. Advanced open-source data formats enabling simplified, efficient and agile storage, access and publication of large-scale volume and multidimensional datasets will be of interest for the beamline, and vice-versa: CORUS can play a role as an early adopter and advocate of such next-generation consensus data formats and processes of volume microscopy data and metadata[165, 166]. Finally, collaborative efforts with the Instruct Imaging Processing Center (I2PC) in Madrid could prove advantageous, particularly with respect to the joint development of software and the standardization and simplification of image processing tasks.

Concluding remarks

The proposed CORUS beamline at ALBA-II synchrotron will house the **nanoImag** end-station, a nano X-ray microscope operating at three fixed energies (10 keV, 19 keV and 27 keV), and the **nanoSpec** end-station, a nano X-ray microscope with spectroscopic capabilities (from 4 keV to 27 keV). Both instruments will be specifically designed to operate under cryogenic conditions, which is crucial for preserving the ultrastructure and native chemical composition of cells. They will enable the characterization of biological materials in near-to-native conditions, minimizing artifacts associated with chemical fixation and dehydration.

The **nanoImag** end-station will facilitate two main programs: 2D and 3D cryo nano X-ray fluorescence (XRF) and 3D cryo or room temperature phase contrast imaging (PCI). The cryo-nano-XRF program will allow imaging and quantification of trace metals and oligoelements in whole cells or tissue sections with high sensitivity (ppm). The cryo/RT PCI program will reveal the ultrastructure of cells, organoids, or soft tissues using tomography stitching for large volumes in the mm^3 range. The **nanoSpec** end-station will enable 2D and 3D chemical speciation determination at the subcellular level.

The techniques promoted by both end-stations operating under cryogenic conditions are complementary and their design will allow, by easy sample transfer, multimodal correlative approaches to retrieve the maximum amount of information possible (from these X-ray-based microscopy approaches) from the same specimen, therefore promoting a better understanding of the complexity of biological systems in metallomics, pathogen-host interactions, metal nanocomposites, toxicology, tissue organization, biomineralization, bioremediation strategies, food security and sustainable agriculture, among others.

Minimum radiation dose strategies will be required especially for 3D XRF and spectromicroscopy. Developing smart acquisition methods and algorithms incorporating sample sparsity handling will be mandatory to produce meaningful data. This is of utmost importance when correlative approaches are considered.

CORUS will have several advantages over competing tools. **NanoImag** will excel at imaging oligoelements (e.g., Ca, Mn, Fe, Co, Cu and Zn) at 10 keV while also allowing the detection of 2nd row transition metals (e.g., Ru, Rh, Ag and Cd). **NanoSpec** will be a unique tool in Europe allowing cryo speciation with 2D and 3D capabilities at a focus better than 50 nm.

The potential impact of this advanced instrumentation will promote collaborations within ALBA through correlative or/and multimodal approaches with MISTRAL, MIRAS and FaXToR, as well as with larger national initiatives such as the advanced cryo-electron microscopy infrastructures (JEMCA at ALBA, CNB-CSIC in Madrid and Biofisika in Bilbao). ReDIB and CIBER networks can foster knowledge sharing and identify new applications in biomedical research. Collaboration with the Instruct Imaging Processing Center will aid in data processing and software development. Finally, CORUS can become the cornerstone of the project REACH-OneHealth, now being prepared by ALBA and partners, which will aim at societal *bio-preparedness* to effectively mitigate the threats for health, food and environment from changing worldwide conditions. CORUS is fully compatible and complementary to the biosafety level 3 capabilities that the project is proposing.

In summary, CORUS will be at the center of the Life Science research at ALBA-II, which capabilities will cover biological X-ray imaging from 20 nm to the micron scale spatial resolution, across fields of views covering from single cells to mm^3 landscapes describing entire tissue microenvironments, strengthening the relevance of the scientific results by definitively linking function, elemental distribution, speciation and structural information and, in the end, delivering new insights and solutions to societal challenges.

2. User community

As detailed in the scientific case, CORUS nanoprobe will impact the Health, Food and Environmental research in Spain, Europe and beyond. **62 supporting Principal Investigators** (including co-proposers) of **46 Research Institutes** (27 from Spain, 10 from France, two from USA, one from Italy, one from Israel, one from Portugal, one from Switzerland, one from UK, one from Brazil and one from Japan) are supporting the CORUS proposal as of today, and these numbers will undoubtedly increase once this new beamline becomes a reality. The strong support received during the proposal phase demonstrates the interest of a broad, multidisciplinary user community towards cryo nano-XRF, cryo nano-XANES and nano holotomography. It is worth noting that some of the supporters are already ALBA users, which reinforces

the strategy of proposing CORUS to fill the missing elemental cellular information and the multiscale gap imaging (between MISTRAL and FAXTOR) of current ALBA capabilities, promoting correlative imaging approaches at multiscale level for better understanding the complexity of biological systems. An exhaustive list of supporting Principal Investigators is included in section 7.

The supporting research groups dedicate their efforts towards the understanding of the following topics:

● the design and study of therapeutic and biotechnological agents like metallodrugs, catalysts, synthetic proteins or nanomaterial (CICBiomagune, DIPC, IMDEA, UAM, ICMM & IBBTEC),

● the study of metallomics and related diseases (Universidad de Valencia, INCLIVA, UAB, IBMB, IIS La Princesa, INSERM-Grenoble, CNRS-Bordeaux, ESRF, Institut Pasteur & Nagoya University),

● pathogen infections and novel antibiotics (CNB, CIB, UPC, INRAe, INSERM-Aix-Marseille, ITQV-Nova, Fiocruz, Institut Pasteur & SOLEIL),

● tissue organization to understand the connectome, neurodegenerative or pulmonary vascular diseases, cardiovascular changes and injuries associated to aging and/or genetic alterations (IRB, IDIBGI, IDIBAPS, Achucarro, CICBiomagune, CBM-Severo Ochoa, Instituto Cajal, UAB, Hospital Sant Joan de Deu, EMBL-Barcelona, Francis Crick Institute, ESRF, INMED, SLS & APS),

● biomineralization (Universidad del País Vasco, Bioscience and Biotechnology Institute of Aix-Marseille, Université de la Sorbonne, UNIBO & Weizmann) and finally,

● plants, soil contamination and bioremediation (MNCN, IMIDRA, CNAG, INRAe, ESRF & Los Alamos National Lab).

This research diversity is unequivocally one of the strengths of CORUS, as this unique nanoprobe can indeed produce essential results to face major societal challenges such as defined by the World Organisation for Animal Health in the *One Health* approach (https://www.woah.org/en/what-we-do/global-initiatives/one-health/).

3. Technical Proposal

The optical design and managerial aspects below are preliminary. The final design and aspects of the project management will need to be revised by the ALBA scientific, engineering and management teams once CORUS is approved.

Photon source

CORUS is conceived to be fed by an insertion device in the ALBA-II lattice, which is the optimal photon source for a beamline aiming to have a nanometer-sized X-ray focal spot. Nevertheless, the current ALBA lattice could also provide a useful beam for commissioning and first testbench experiments, should the beamline receive the X-ray beam before the dark period. The insertion device is proposed to be an in-vacuum undulator with a magnetic period of 19 mm and inserted in the port BL04 (Table 1). This port maximizes the overall length of the beamline up to 275 m, thus reducing the size of the focal spot at the two CORUS end-stations and allowing a larger working distance between the last optic and the sample position. Still, the beamline is also compatible with available port BL02 if the length of the nanoImag end-station is reduced to 240 m. Assuming a magnetic gap of ~4.5 mm, which is feasible in a 4th generation source, the IVU19 provides the photon energy tunability required for the nanoSpec end-station, with a high flux over the targeted spectral range of the beamline, between 4 and 27 keV (Fig. 5).
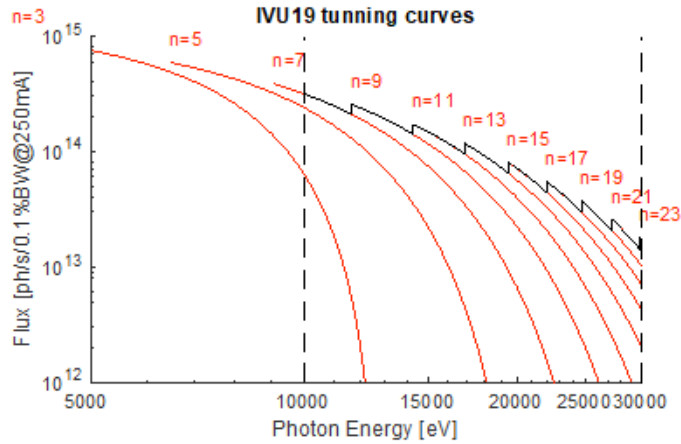
Figure 5. Tuning curves of the proposed in-vacuum undulator IVU19

Parameter	Value	Comment
Magnetic period l_U	19 mm	Full tunability between 4 and 27 keV is required.
Magnetic length L_U	2 m	Could be larger depending on the storage ring lattice.
Beam size (>5 keV)	14×14 ⬜m	Limited by the electron beam.
Beam divergence (>10 keV)	21-24 ⬜rad	Limited by the electron beam dispersion and diffraction.

Table 1. Main parameters of the CORUS photon source

Beamline optics

The proposed optics that will feed the two end-stations, nanoSpec and nanoImag, are based on two focusing stages, using either total reflection mirrors or multilayers (Fig. 6). The first focusing stage is used for both end-stations and consists of a pair of total reflection cylindrical mirrors oriented horizontally. M1 mirror has a meridional radius to focus horizontally, while M2 has a sagittal one to focus vertically (Table 2). Both mirrors are coated with Ir and have a grazing incidence angle of 2.5 mrad.

The beam is monochromatized with dedicated instruments for each end-station. The beam directed to **nanoSpec** is filtered by means of a double crystal monochromator (DCM) using the Si(111) reflection and a second one offering a higher energy resolution at the expense of flux. The DCM is removed from the beam path when the beam is directed to **nanoImag**. Next in line comes the water-cooled, multilayer mirror M3, which removes most of the power and deflects the beam by 1.548 deg to the nanoImag station. M3 will have three W/B_4C multilayer stripes with bilayer spacings of 4.49, 2.42 and 1.70 nm to filter the beam energy at 10, 19 and 27 keV, respectively, with a bandpass of $\gtrsim$1%. This choice, together with the fine adjustment of the mirror pitch, will allow to have the same beam path for all the energies. The M3 mirror is withdrawn from the beam path when the nanoSpec end-station is used.

All these elements are included in a first optical hutch. The optical layout of CORUS (Fig. 7) is compatible with the existing one enclosing the optics of the BL04-MSPD beamline, currently in operation at ALBA. The compatibility with this existing infrastructure, together with the reduced dimensions of the second optical hutch, will dramatically reduce the cost of the required radiation enclosures, which is currently very high, and the electronics infrastructure.
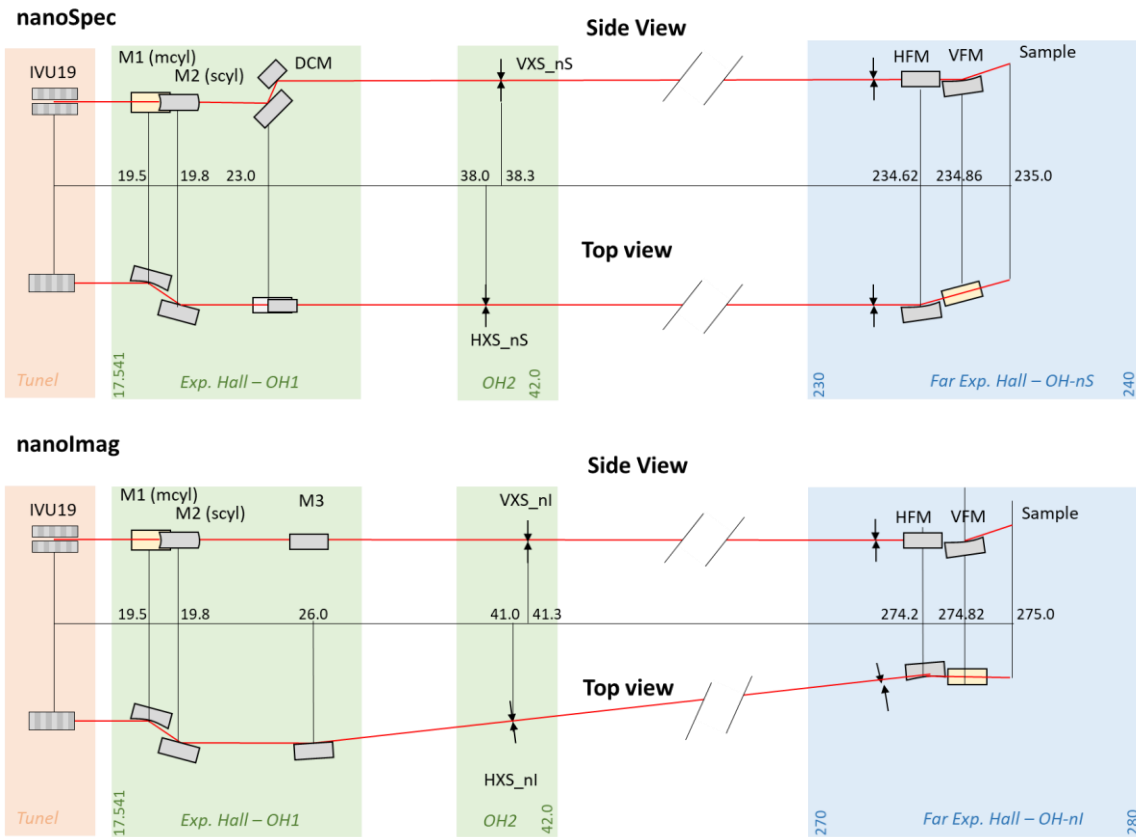
Figure 6. Beamline optics for CORUS beamline for the two branches **nanoSpec** (top) and **nanoImag** (bottom).
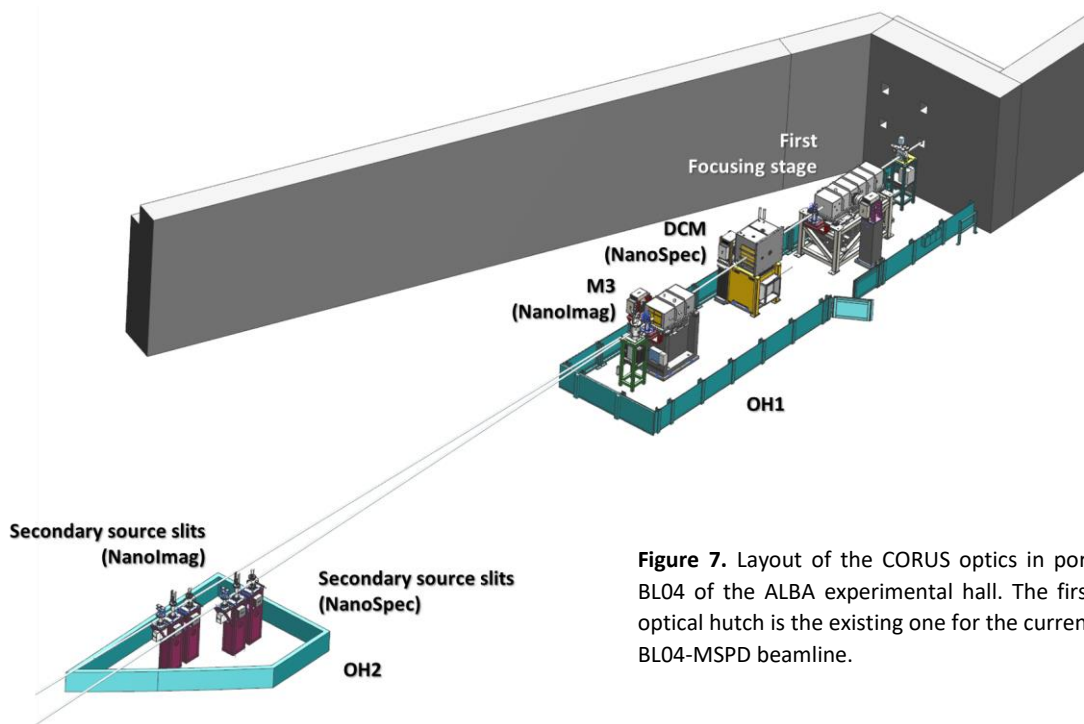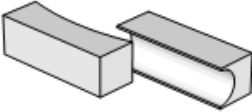

Figure 7. Layout of the CORUS optics in port BL04 of the ALBA experimental hall. The first optical hutch is the existing one for the current BL04-MSPD beamline.

Parameter	M1 mirror	M2 mirror	Comment
Focusing concept/ Figure	Horizontal focusing Meridional radius	Vertical focusing Sagittal radius	
Optical length	400 mm	400 mm	<100 nrad rms slope error
Radii	8052 m (meridional)	49.99 mm (sagittal)	M1 meridional /M2 sagittal radii

Table 2. Main parameters of the first focusing stage, which is common to both end-stations.

The beam emitted by the source is focused by the first pair of mirrors (M1 and M2) onto the secondary source slits, which are specific for each branch (VXS & HXS in Fig. 6). M1 and M2 are both horizontally deflecting, in opposite directions. M1 is a meridional cylinder, which focuses the beam horizontally onto HXS, and M2 is a sagittal cylinder that focuses the beam vertically onto the VXS. The selected configuration of the mirrors allows for high stability of the beam without introducing any vertical deflection. Given the small footprint of the beam on the mirrors (~180 mm), there is no noticeable aberration of the wavefront.

The slits HXS and VXS for each branch are placed at the edge of the critical slab of the experimental hall, in the main building of ALBA. They are enclosed in a dedicated small hutch with convenient radiation isolation. The beam is transported from the first optical hutch by lead-shielded flight tubes 10 m in length.

The beamline does not have any other deflecting optics between the secondary source slits and the end-stations, and the beam propagates to the **nanoSpec** and **nanoImag** end-stations, placed at 235 and 275 m from the source, respectively. These distances can actually be adjusted with limited impact on the beam performance in case any aspect of the project, such as the budget or the infrastructure, would require it.

The refocusing stages, which image the secondary source onto the sample, consist of a pair of elliptical cylinder focusing mirrors with fixed curvature in Kirkpatrick-Baez (KB) configuration (Table 3). In the case of the **nanoImag** end-station, there are three graded multilayer KB pairs tuned at 10, 19 and 27 keV, respectively, and mounted on a linear translation stage to select them. In the case of **nanoSpec**, there are two KB pairs working in total reflection, with different coatings and incidence angles to cover the entire energy range of the beamline. The ellipse radii and the grazing incidence angle along the surface are kept within feasible values using the current technology. The focusing distances will be small due to the high demagnification needed to achieve a nanometric beam size at the focal position. The working distance - the distance between the end of the last mirror and the sample position - is only 40 and 50 mm for the **nanoImag** and the **nanoSpec** end-stations, respectively. Therefore, these optics are included in the vacuum vessels enclosing the end-stations.

	nanoImag (3 KB pairs)	nanoSpec / low Energy	nanoSpec / high Energy
Lay out	HFM VFM 202.5 122.5 80 80 40 165 120	HFM VFM 347.5 227.5 120 140 50 315 190	HFM VFM 382.5 245 137.5 175 50 315 225
Energy	10 / 19 / 27 keV	4-11 keV using Si(111) 6-11 keV using Si(400),(311)	10-27 keV
Incid. angle	1.18 / 0.89 / 0.69 deg	5.5 mrad	2.8 mrad
Surface material	Graded multilayer W/B_4C 3.0 / 2.1 / 1.9 nm	Rh coating	Ir coating
Object distance (HFM / VFM)	233.2 / 233.023 m	196.42 / 196.56 m	196.42 / 196.56 m
Image distance	202.5 / 80 mm	347.5 / 120 mm	382.5 / 137.5 mm
Length (H/VFM)	165 / 80 mm	315 / 140 mm	315 / 225 mm

Table 3. Characteristics of the KB focusing stages for **nanoImag** and **nanoSpec** (low and high Energy range).

Beam characteristics at sample position

Assuming ideal optical surfaces, the focal beam size is limited mainly by the numerical aperture of the optics at low energies and by the geometric demagnification of the intermediate source at high energies. However, when considering real optics, wavefront propagation modelization[167] shows that the minimum spot size is limited by the surface errors of the refocusing optics. To mitigate this effect, for all the KB mirrors, the height error cannot exceed 1 nm peak-to-valley, while the slope error must stay below 80 nrad rms. These values are currently at the limit of the field, and are expected to slightly improve by the time the beamline is built. Assuming these values, the spot size for **nanoImag** ranges between 11 and 18 nm FWHM while for **nanoSpec** lies in the range 30-50 nm FWHM (Table 4, Fig. 8).

	nanoImag	nanoSpec
Beam size	11-18 nm	30-50 nm
Depth of field (limited by last KB mirror)	5 µm	30 µm
Energy range	10, 19, 27 keV	4-27 keV
Energy bandwidth (ΔE/E)	$\gtrsim$1%	Si(111), $2 \cdot 10^{-4}$ / Si(311), $8 \cdot 10^{-5}$ / Si(400), $4 \cdot 10^{-5}$

Table 4. Beam properties at sample position for both end-stations
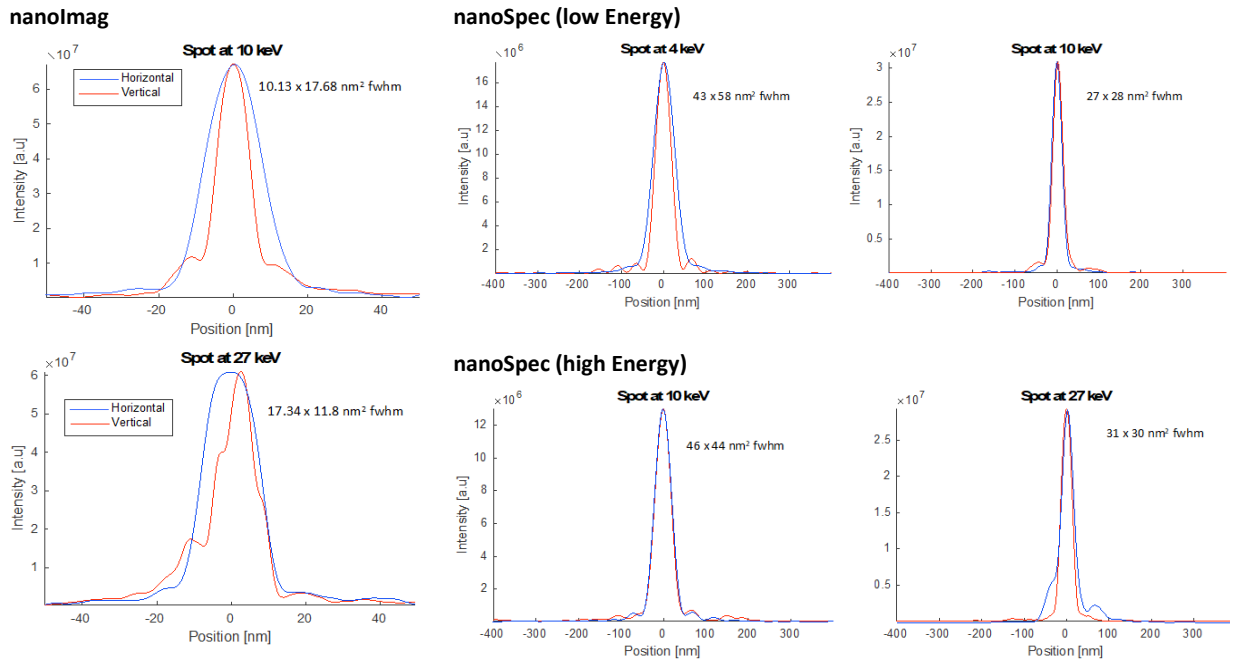
Figure 8. Beam spots of **nanoImag** and **nanoSpec** end-stations assuming state-of-the-art figure errors of the KB mirrors (height error 1 nm PV, slope error 80 nrad rms).

The KB of the **nanoImag** end-station is particularly demanding. Here, the depth of field (DoF) is extremely short, below 5 µm for the VFM and about 10 µm for the HFM (Fig. 9). At low energies, the spot and divergence are dominated by diffraction effects, while at high energy configuration the slope error determines the light distribution in-focus and out-of-focus. The beam divergence is about 7.9 and 4.9 mrad at 10 and 27 keV, respectively.
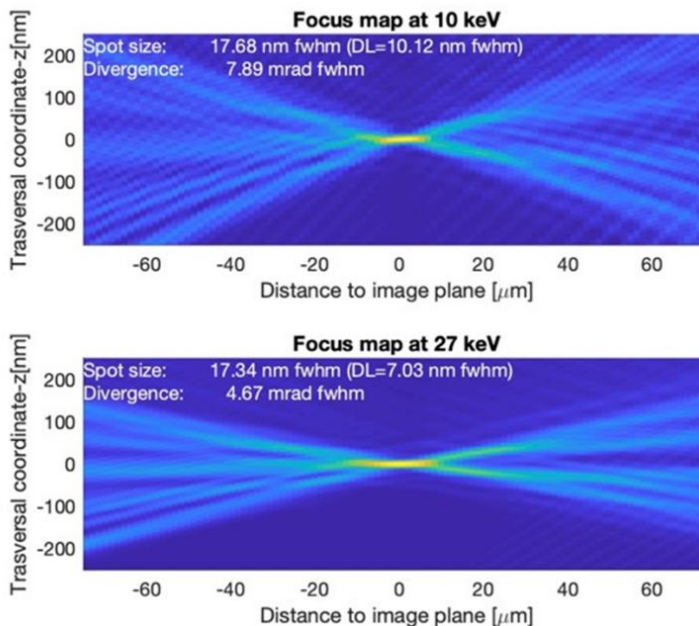
Figure 9. Depth of field of the refocused beam at the sample position of the nanoImag end-station. The inhomogeneities of the beam are caused by the assumed mirror figure errors (1 nm PV height error, 80 nrad rms slope error).

The flux at sample is essentially driven by the photon energy bandwidth and the reduced acceptance of the KB mirrors. In the case of **nanoImag**, including the effect of the wide energy bandpass around 1% and 0.7 reflectivity, and the limited acceptance of the mirrors, the flux can be as high as $2.24 \cdot 10^{13}$ ph/s at 10 keV, while still high at 19 and 27 keV, for which the attained fluxes are $4.58 \cdot 10^{12}$ ph/s and $7.64 \cdot 10^{11}$ ph/s, respectively[167].

The flux at sample for nanoSpec depends on the KB pair and the reflection used to monochromatize the beam. Taking into account the nominal relevant factors, the Si(111) reflection flux figure can be as high as 10^{12} ph/s using the low energy KB, while above 12 keV the flux is in the 10^{11} ph/s range, decreasing with photon energy (Fig. 10). The high calculated values of flux at sample offer the possibility to include a second pair of crystals in the monochromator using a reflection with a narrower bandpass, to be used in experiments requiring a high energy resolution to determine the oxidation states of specific elements present in the sample. For instance, the flux obtained with reflection Si(400), which delivers an energy bandwidth 5.3 times narrower than Si(111) and a flux reduced by the same amount. The obtained flux with Si(111), in the 10^{11}-10^{10} ph/s range, is suitable for most nano-XANES experiments, for which fluxes around $3 \cdot 10^9$ ph/s can still be used. A higher flux and intermediate bandwidth resolution can be obtained using the Si(311), for which both the bandwidth and the flux are narrowed and reduced, respectively, by a factor 2.4 compared to (111).

Harmonic suppression is important in the **nanoSpec** end-station. This is achieved by the proper selection of the KB mirrors and by the systematic extinction of the second harmonic in the case of reflections (111) and (311). In any case, due to the small d-spacing, the reflection used to obtain high energy resolution will likely not deliver a beam with a photon energy lower than ~6 keV, which relaxes the conditions in which the harmonics must be suppressed.
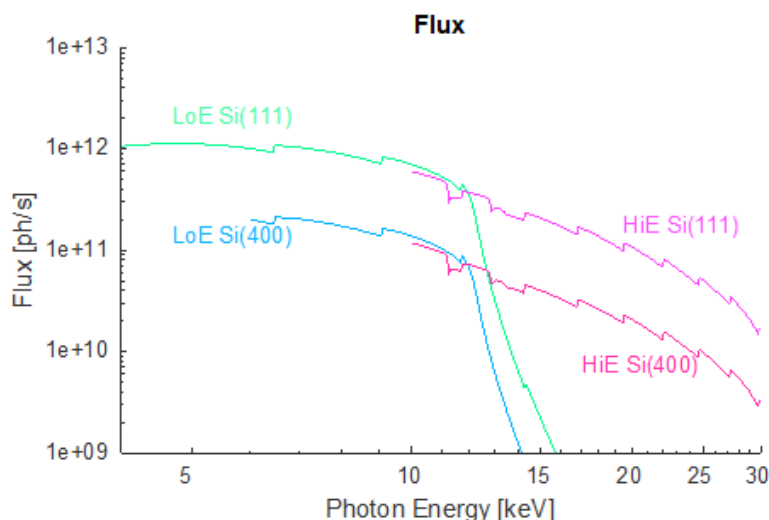
Figure 10. Flux at sample of the nanoSpec end-station taking into account the energy bandpass, the reflectivity and the limited acceptance of the mirrors. The flux obtained using the Si(400) reflection is also shown.

Importantly, the layout of CORUS is compatible with the constraints imposed by the terrain and the limits of the available land premises (Fig. 11). The overall length of the end-stations can be fine-tuned upon the floor constraints that may appear in the design or the construction phases.
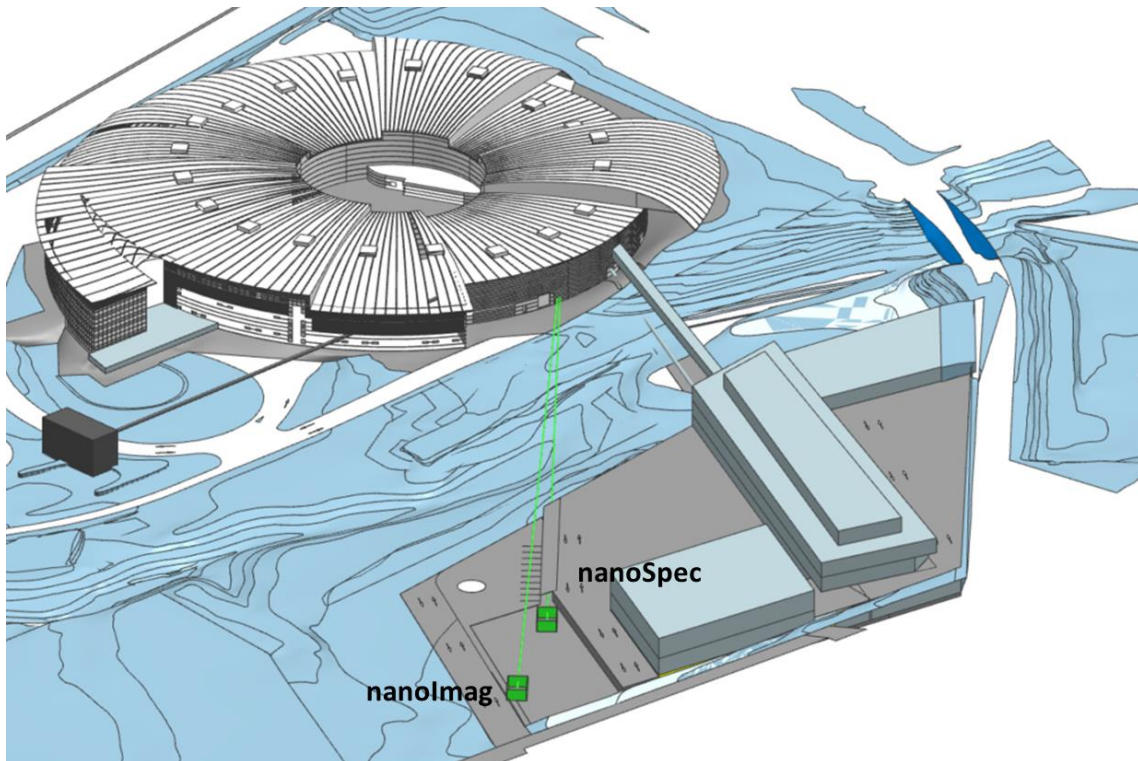
Figure 11. View of the CORUS end-stations in the available land plot.

End-stations

CORUS will house two in-vacuum (10^{-8} mbar) end-stations with cryogenic capabilities, **nanoImag** and **nanoSpec**, which are detailed below. **NanoImag** requires the highest possible brightness and stability to achieve an ultimate nanofocus of ideally 11-18 nm with the highest possible flux at three fixed energies: 10 and 27 keV are suited for X-ray fluorescence, while 19 keV will be used for phase contrast-based imaging (larger transverse coherence length). Complementary to this, **nanoSpec** will be the first cryo spectroscopic end-station in Europe, covering the range 4-25 keV, with a stable nanofocus of 30-50 nm and energy tunability with $\Delta E/E = 10^{-5}\text{-}10^{-4}$.

The end-stations will have a similar sample environment but each of the vacuum vessels will contain specific nanofocusing optics, similar to ID16A[148] at the ESRF, as already mentioned above. We aimed at working distances of 40 mm and 50 mm for each end-station, which implies space constraints but is manageable such as at ID16A (*e.g.*, 35 mm of working distance).

To ensure high thermal and mechanical stability, the end-stations will be located in two separate experimental hutches with temperature control of 23.00 ± 0.03° C. The separation allows each of them to be accessible when the other is being operated. A slab will limit vibrations and relative movements of optical elements. Furthermore, primary pumping should be brought from a technical building outside the experimental hutch.

The challenge of designing nanoprobe[168] end-stations is achieving high resolution, high accuracy positioning and scanning of the sample with long term stability (invar parts will be required) during rotation in vacuum and at cryogenic temperatures. In addition, the space around the sample should be sufficient to accommodate a cryo gripper for sample exchange (similar to MISTRAL), X-ray fluorescence detectors and an objective lens for the visible light microscope required for both navigating within the

sample and locating specific regions of interest benefiting from visible light fluorescence tagging of intracellular organelles or molecules.

Constant active feedback will be required to correct the run-out online at the sample position with 5 nm accuracy and keep the sample at the rotation axis and in the focal plane within the DoF. Capacitor sensors could be used to measure displacements. We will be targeting XRF dwell times of 5 ms/point or better and stage motor speeds of 40 mm/s with a feedback loop frequency of at least 200 Hz. Cryogenic temperatures will be achieved with a cryo finger located vertically, parallel to the axis of rotation and below the sample, to accomplish the smallest possible run-out at the sample position, in addition to avoiding blocking space around the sample. Insulation between room temperature parts and cryogenic parts will be needed, as well as temperature monitoring.

A multiple sample system will be implemented in both end-stations such that several samples can be loaded at a time, and stored in vacuum and at cryogenic temperatures (similar to MISTRAL). Sample storage is essential to optimize loading times and to allow users the possibility to exchange samples in vacuum without the need of the scientific beamline team. Samples on a cryo shuttle will be loaded into the vacuum chamber of the end-stations through a vacuum load-lock, which will be pumped to 10^{-6} mbar, thanks to a specific transfer chamber that allows transport of the samples at cryo and under vacuum from the biology laboratory to the end-stations (similar to MISTRAL). All sample holders will share the same lower part for transfer and mounting into the end-stations (ideally compatible with MISTRAL). Both end-stations will be specifically designed for cryo but room temperature experiments will also be feasible. Regarding operation, cryogenic beamtime campaigns and room temperature ones will be conveniently scheduled to favor instrument stability.

For nano-XRF and spectroscopy the sample will be positioned at the focal plane of the KBs while for phase-contrast based imaging the sample will be positioned after the focus. In the case of holography (2D or 3D), four distances will be used and the focus-to-sample distance (z_1) will be varied while the detector will be kept fixed (z_2). The change in magnification, $M = (z_1+z_2)/z_1$, due to the divergent beam will be corrected for since the field of view varies with z_1. The phase retrieval procedure will exploit the difference in effective propagation distance $(z_1 \times z_2)/(z_1+z_2)$. For tomography, sample rotation of 180 degrees will be available and voxel sizes of 10 to 150 nm will be targeted. Note that in the case of using flat sample supports, a missing wedge is unavoidable (such as in cryo-SXT at MISTRAL or cryo electron tomography).

A preliminary mechanical design of the end-stations should consider the following needs: 1) a large stroke translation along the beam direction to accommodate the distances used in nano holotomography (only for **nanoImag**) and the gripper for sample exchange; 2) a vertical translation stage for sample alignment and navigation; 3) height/pitch/roll will be required to align the rotation axis orthogonal to the beam axis of the KBs; 4) short-range piezo actuators will be needed to actively correct for the run-out at the sample position; 5) a high precision rotation stage; 6) fine sample stages to center the sample on the rotation axis.

To locate specific cells on the sample support or tissue regions, a visible light microscope (VLM) with brightfield and reflection modes, as well as epifluorescence, will be used in both end-stations. This will make use of convenient fluorescent tags or proteins to pinpoint cellular organelles or molecules that indicate cellular status during infection processes, specific location of targeted molecules, etc. (similar to MISTRAL). This VLM will have an in-vacuum long working distance objective (20X at least or better), while filters and LEDs will be outside the vacuum chamber. The VLM will allow an efficient use of the beam by re-locating specific regions of interest that would have been mapped at higher resolution (50X or 100X) in the supporting biology laboratory (same workflow as for MISTRAL), or elsewhere, prior to the beamtime (see below section "Sample preparation and security"). The focus of the VLM will have to match the KBs focal plane.

Regarding detection, nano X-ray fluorescence requires energy dispersive solid-state detectors with large solid angle for efficient collection and high throughput. Since low Z elements (*e.g.*, Mg, P, S, etc.) are important for cellular imaging and have to be well detected, low absorbing detector windows such as those made with thin Be will be needed. Two silicon drift detectors (SDD) will be located at 90 degrees at each side of the sample in both end-stations. Compact in-vacuum solutions with a long detector nose should also be privileged due to foreseen space constraints around the sample. For instance, the Vortex ME-7 from Hitachi with 7 square sensors each or the ARDESIA development[169] with 16 channels could be considered. For ppm-level elemental detection, spectral performance in terms of purity and peak shape are essential, as well as energy resolutions better than 140 eV.

For the phase contrast (PC) imaging, a spatial resolution of 20 nm will require a pixel size smaller than 10 nm, therefore resulting in fields of view of about 50 μm at the focal plane for a 6144^2 pixel detector. An indirect detection scheme with a scintillator screen whose luminescence image is magnified by visible light optics (with a numerical aperture as large as possible) onto an image sensor such as a sCMOS will most probably be used (high definition sensor, 10 μm pixel size, 6144^2 pixels, low noise, tens of frames per second). Thanks to the X-ray magnification, the absolute spatial resolution requirements are relaxed, but the focus-to-detector distance needs to be kept reasonable at 1.2-1.5 m, so small pixel sizes are favored (effective pixel sizes of 1 μm with 10X magnification).

In the case of spectroscopy, both absorption and fluorescence modes will be available, being the latter favored for biological samples. For absorption mode, a Si photodiode will be used.

Finally, detectors are constantly evolving and possibilities will be evaluated at the needed time, once CORUS is funded and during the detailed design period of the beamline.

Data acquisition, management and computing needs

The addition of new beamlines at ALBA-II will result in an increase of data collection rates. To provide a more quantitative overview, ID16A-ESRF has estimated 5TB/day of average output [170]. Advances in detectors and higher scanning speeds may contribute to increasing this output further. Therefore, solutions must be found to develop automatic data pipelines. In terms of IT infrastructure, each branch will need at least 40 dedicated online CPU cores and access to an HPC infrastructure. Managing daily TB-size data activities, such as streaming, reconstruction, analysis, and storing, is challenging. As already in place for the current beamlines under construction, XAIRA and FaXToR, the IT group is working on the development of scalable and sustainable solutions for ALBA-II. In addition, automatic procedures for sample exchange in the main vacuum chamber should also be considered for both end-stations, minimizing human intervention.

CORUS aims at providing correlative experiments, and the data management must comply with them. The solutions need to be unified, not only between **nanoImag** and **nanoSpec**, but also with other beamlines (MISTRAL, MIRAS and FaXToR), whenever possible. Raw data will be converted to HDF5 files, following the NeXus convention for field names, attributes and their organization (as already implemented at ALBA) [171]. A unified solution will provide not only common data format, but also plug-ins for dedicated processes such as data transformation and reduction, in accordance with the different beamlines and technique requirements. For CORUS, the solution must combine XRF, PC imaging and VLM in a unique workflow for data management, processing and storage. Open source python packages will be used for data analysis, such as PyMCA[172] to fit the fluorescence spectra and perform a quantitative analysis. PyHST[173] for iterative reconstruction methods will be used for 3D tomographic reconstruction of the retrieved phase maps. For holotomography, the reconstruction will be performed by employing PyPhase[174], a modular open-source phase-reconstruction package. As holograms will be collected in cone-beam geometry, they will be

interpolated to the largest magnification and smallest field of view before phase retrieval. In addition, alignment of the rescaled holograms by subpixel image registration will be needed.

Compressed sensing strategies for data reconstruction and analysis will benefit all techniques. This will be applied in XRF mapping of very large areas, such as wide scale brain imaging[175, 176] for instance, or in spectromicroscopy[177, 178]. Such approaches will substantially reduce scanning time allowing to decrease the acquisition time in the areas containing background while increasing it in the regions of interest. Compressed sensing will be further used for optimizing the 3D reconstructions of a reduced number of projections to keep the dose within limits, while preserving spatial resolution [179].

Specifications of beamline control system.

The control system for all instrumentation motors and data acquisition at ALBA is based on SARDANA[180]. The sample positioning needs to be controlled prior and during the acquisition. In detail, the VLM will focus the KB focal plane while moving the alignment and scanning motors to locate the specimen in the relevant position with respect to the X-ray beam, prior to acquisition. Access to the fine stage control will be done through dedicated servers, allowing a setpoint change of the stroke (transverse to the impinging X-ray beam direction) based on the acquisition modality. The triggering for synchronization will be given most probably by the sample stage. The end-stations operating at cryogenic temperature will benefit from high accuracy sample nano-positioning and scanning stages under the control of capacitor sensors. These sensors guarantee the sample position at all times. In addition, temperature sensors will be required to monitor and retrieve the temperatures at the sample position and all along the cold path, which includes sample storage in the shuttle and gripper. If heaters would need to keep specific parts of the end-station at room temperature, these would also need to be controlled. The diagnostic elements will further ensure monitoring of any drift of the KB mirrors leading to misalignment of the focal plane onto the rotation axis. Note that the smallest DoF will be of about 5 μm, and the sample needs to be centered in the DoF all the time, when located at the focal plane. During 2D and 3D measurements, the sample position will be automatically corrected by monitoring its displacement thanks to these capacitor sensors. All critical positions will be saved in log files, in order to easily retrieve potential sources of alignment errors.

Sample preparation and security

Cryogenic preparation is mandatory when imaging fixed cells in order to keep them in close-to-native conditions, preserving the ion distribution, structure and chemical state. Therefore, the samples will be vitrified in amorphous ice by plunge freezing or high pressure freezing. Convenient sample supports will be used to reduce X-ray fluorescence background keeping in mind that correlative imaging (*e.g.*, VLM, MISTRAL, MIRAS, cryo-ET) is required to exploit all possible information for a specific sample and therefore is a mandatory goal.

Biosafety level (BSL) 2 samples will be imaged. Therefore, a nearby BSL2 laboratory will be required to mount the vitrified samples onto the sample holders keeping cryogenic temperature at all times (100 K). For this, a dedicated liquid nitrogen workstation will be used (similar to MISTRAL). A cryogenic transfer vacuum chamber (similar to the MISTRAL one) will be needed to transport the samples from the laboratory to the end-stations. The BSL2 laboratory will be equipped with necessary instrumentation to ensure all the steps of the sample preparation, such as those in the current MISTRAL BSL2 laboratory. Users will be allowed to use the laboratory prior to their beamtime for sample preparation. For sample screening and correlative imaging purposes, a VLM with a convenient cryo-stage will be available at the BSL2 laboratory. This will allow selection of the best samples to be imaged with X-rays, as well as mapping these at high resolution (50X or 100X) for correlative approaches (same workflow as for MISTRAL).

For biological soft tissues, it has been shown that heavy metal staining protocols optimized for volume electron microscopy (EM) are compatible with hard X-ray tomography, including nano holotomography[98], enabling broader workflows compatible with follow-up volume EM at targeted regions of interest. This approach efficiently generates samples on the mm^3 scale with sufficient preservation of the tissue ultrastructure, which can be quality-controlled with EM ahead of synchrotron imaging, and is highly translatable to other tissues already being studied with volume EM[181]. In order to obtain sub-100 nm resolution, however, the necessary X-ray doses might conflict with the resilience of the embedding materials to mass loss: $6 \cdot 10^8$ Gy in the case of PPMA at cryogenic temperatures[182] or the recently used trifunctional resin withstanding doses beyond 10^{10} Gy. Even so, transient morphological changes (dilations) can occur and non-rigid tomographic reconstruction strategies may provide resilience to it. Moreover, sample geometry can also have an influence on the final resolution, with cylindrical samples being optimal for tomographic reconstructions[183], and in some applications it might be desirable to generate multiple samples from a sub-mm neighborhood of a given specimen. Ultramicrotomy can provide reliable approaches to trim a single targeted prism sample from a larger specimen[184] and lathe systems can provide means to obtain cylindrical profiles[185]. Obtaining multiple samples per specimen at targeted locations can be achieved by FIB-SEM, or more effectively using femtosecond laser milling[186].

Finally, certain ethical and legal frameworks will be necessary to handle tissue biopsies of human origin, biological material of regulated animal species or of genetically-modified organisms. Similarly, some pre-established risk assessments that cover common workflows across broad disciplines would be beneficial, such as those that apply when imaging heavy-metal stained biological tissues (which may contain traces of Os, Fe, U and Pb) embedded in resin, or samples with localized metal distributions (*e.g.,* radioisotopes).

Management of radiation damage

Radiation damage induced by the deposited X-ray dose is the ultimate limitation in terms of achievable spatial resolution. Minimum radiation dose strategies will be required especially for 3D XRF and XANES at cryogenic conditions. A combination of detector efficiency, smart acquisition methods and algorithms incorporating sampling sparsity handling (compressed sensing schemes)[177], as well as dose fractionation will need to be extensively explored to find the minimum dose working conditions to be applied for each technique. Monitoring the accumulated dose will be mandatory to produce meaningful results and validate experimental strategies in particular when correlative workflows, exploiting the maximum possible information on a specific sample, will be considered.

4. Risk Management

The following table summarizes the technical risks for the CORUS beamline.

Risk	Description	Probability	Impact	Mitigation
		Optics		
Floor stability	ES floor slab is recent and different from optics slab, leading to relative movements of BL components	+	+	Construct the ES slab in advance, monitor floor, optical elements able to correct displacements
SR stability	New lattice, emission point may be different from nominal	+	+	SR correction, optical elements able to correct displacements

Optical elements stability	Long lever arms make the BL optics prone to spatial instability. Especially critical in the DCM for nanoSpec	++	++	Use of a secondary source, install interferometers to monitor and feedback
Multilayer optics	Degradation of multilayers upon power load, as observed in other nanoprobe beamlines.	++	+	First optics not based on multilayers, replacement of multilayers, select radiation resistant elements, reduction of flux
End station				
New technologies	Technologies in positioning and feedback systems new to ALBA	+++	++	Build up in-house know-how. Externalize critical components
Cryogenics in sample stages	Stability of optics and sample	++	++	Build up in-house know-how. Externalize critical components
Temperature, humidity control	End stations require stabilities of ±0.03° C in temperature and 1% in relative humidity	++	+	Automatize sample loads/unloads, efficient HVAC, pre-conditioning area before experimental hutches
Carbon footprint	Hutches infrastructure outside the main building	+	+	Infrastructure isolation allowing for moderate energy consumption

5. Budget based on main components

CORUS budget (see below) has been calculated from the current ALBA beamlines in construction ("BASE" column). 5% per year has been added to account for price increase ("ADDED" column), in addition to 10% of contingency. The grand total without considering civil works and the computing infrastructure is estimated to ~15,9 MEuros. Note that CORUS could benefit from the optics hutch of BL-04MSPD, once this beamline is relocated. This would decrease the estimated budget by about 0.5 MEuros.

	BASE	ADDED	TOTAL (k€)	Justification
ID	1750	0	1750	3SBar (2023)
FE (FE+Absorbers+vac,chambers)	280	100	380	FAXTOR (2021)
BL OPTICS and backbone, including mirrors, gratings, crystals+cryogenics	2027	750	2777	XAIRA + 550 kEUR(mono) + 200kEur (JTEC)
VACUUM (only standard components)	421	450	871	XAIRA + 450kEur (long pipe)
STATIONS (strongly depending on the technique)	3700	3200	6900	XAIRA*2
CONTROLS ELECTRONICS AND INFRASTRUCTURE	802	400	1202	FAXTOR+200 (Tube)+200 (services)
RADIATION PROTECTION	840	200	1040	FAXTOR *1.5 (latest cost is so high)
INFRASTRUCTURE (User Hutches, supports, cooling, AC, light, AC, etc)	289	700	989	FAXTOR*2+400 HVAC
TOTAL BL PROJECTS (incl. 10% contingency)			**15910 k€**	
ITEMS NOT INCLUDED IN THE BUDGET OF THE BL PROJECT				
Computing infrastructure (storage+processing)				
Civil engineering				
Sample preparation Laboratory				

6. Gantt chart with key milestones and main dependencies

The Gantt chart below assumes a starting date on 1st of January 2024. The design and manufacturing periods are extended to account for human resources, which will have to be shared with other projects from the upgrade plan, limiting for instance the publication speed of call for tenders, the capacity of the mechanical engineer group, the tasks that are due by the beamline responsible, etc. In the case of the

end-stations, the duration of the design period accounts for possible in-house developments or the need of prototypes.

The installation of instrumentation in the actual experimental hall is independent of ALBA-II, and therefore commissioning can be started up to the secondary source with the current ALBA machine. The installation of the far experimental hall (FEH) is determined by the finalization of the building, including the experimental hutches of high-density concrete, and is thus tentative. The aim would be to install everything before the dark period to free resources that will be needed during that period. During the dark period, commissioning of the control system and the data pipelines will be performed.

Title	Duration	Start	End
1) Start project		1/1/24	1/1/24
2) Source	3y 4mo 2w	1/1/24	5/2/27
2.1) Design	4mo	1/1/24	19/4/24
2.2) Specs	4mo 2w	22/4/24	23/8/24
2.3) Tender	8mo	26/8/24	4/4/25
2.4) Production	2y	7/4/25	5/2/27
2.5) Delivery		5/2/27	5/2/27
3) Front End	3y 5mo	1/4/24	21/5/27
3.1) Design	4mo	1/4/24	19/7/24
3.2) Specs	5mo	22/7/24	6/12/24
3.3) Tender	8mo	9/12/24	18/7/25
3.4) Production	2y	21/7/25	21/5/27
3.5) Delivery		21/5/27	21/5/27
4) BLOptics	4y 4mo 2w	22/7/24	28/7/28
4.1) Design	1y 2mo 1w	22/7/24	22/8/25
4.2) Specs	6mo	25/8/25	6/2/26
4.3) Tender OptoMechanics	8mo	9/2/26	18/9/26
4.4) Production OptoMechanics	2y 1w	21/9/26	28/7/28
4.5) Delivery		28/7/28	28/7/28
5) Optical Hutch	2y 2mo	25/8/25	20/8/27
5.1) Design	9mo	25/8/25	1/5/26
5.2) Tender	8mo	4/5/26	11/12/26
5.3) Production	9mo	14/12/26	20/8/27
5.4) Delivery		20/8/27	20/8/27
6) Infrastructure OH	3y 2w 4d	27/10/25	17/8/28
6.1) Design+Procurement	1y	27/10/25	25/9/26
6.2) Infr. installation	1y 3w 4d	23/8/27	17/8/28
7) BL installation OH	2y 2mo 4d	24/5/27	24/5/29
7.1) ID+FE	6mo	24/5/27	5/11/27
7.2) Optics	10mo	18/8/28	24/5/29
8) Installation bridge pipe	8mo	11/9/28	20/4/29
9) Endstation	4y 10mo 2w	3/3/25	24/8/29
9.1) Design	2y 2mo 2w	3/3/25	12/3/27
9.2) Tender	8mo	15/3/27	22/10/27
9.3) Production	2y	25/10/27	24/8/29
9.4) Delivery		24/8/29	24/8/29
10) New Building Delivery		30/4/29	30/4/29
11) Infrastructure FEH	2y 6mo 1w	24/5/27	14/9/29
11.1) Design	1y 1w	24/5/27	28/4/28
11.2) Procurement	1y	1/5/28	30/3/29
11.3) Installation	5mo	30/4/29	14/9/29
12) BL Installation FEH	6mo	17/9/29	1/3/30
12.1) Endstation installation	6mo	17/9/29	1/3/30
13) ALBA-II inst. shutdown	1y 7mo 2w 1d	1/1/30	1/7/31
14) Commissioning	3y 1mo 1d	25/5/29	26/3/32
14.1) OH Optics	7mo 2w 1d	25/5/29	21/12/29
14.2) Endstation w/o beam	1y 5mo 2w	4/3/30	4/7/31
14.3) Endstation w/beam	9mo 2w 3d	2/7/31	26/3/32

7. List of Supporting Principal Investigators

The complete list of supporting Principal Investigators, currently 62 of 45 different institutions (excluding the co-proposers) can be found below.

Name	e-mail	Institute
Isabel Castro	isabel.castro@uv.es	Universitat de Valencia, Spain
Juan Antonio Navarro Langa	Juan.A.Navarro@uv.es	INCLIVA/VLC (Instituto de Investigación Sanitaria), Spain
Aitziber López Cortajarena	alcortajarena@cicbiomagune.es	CICBiomagune, Spain
Fernando Lopez	flopez@cicbiomagune.es	CICBiomagune, Spain
Jesús Ruiz Cabello	jruizcabello@cicbiomagune.es	CICBiomagune, Spain
Luca Salassa	lsalassa@dipc.org	DIPC Donostia, Spain
Luis Eduardo Hernández	luise.hernandez@uam.es	UAM, Spain
Ana Pizarro	ana.pizarro@imdea.org	IMDEA Nanosciences, Spain
Olga Caballero	olga.caballero@csic.es	IMN - CNM (CSIC), Spain
Ana Espinosa de los Monteros Royo	anaespinosamr@gmail.com	ICMM, Spain
Fernando Garrido	fernando.garrido@mncn.csic.es	MNCN, CSIC, Spain
Carmen Lobo Bedmar	carmen.lobo@madrid.org	Dept. Investigación Agroambiental, IMIDRA, Spain
Manuel González Guerrero	manuel.gonzalez@upm.es	Centro de Biotecnología y Genómica de Plantas, CNAG, Spain
Montserrat Español	Montserrat.Español@upc.edu	UPC, Spain
Malu Fernández Gubieda	malu.gubieda@ehu.eus	Universidad del País Vasco, Spain
Ana Villar	anavictoria.villar@unican.es	IBBTEC, Spain
Xavier Daura Ribera	xavier.daura@uab.cat	ICREA, UAB, Spain
Marian Oliva Blanco	marian@cib.csic.es	CSIC-CIB Margarita Salas
F. Xavier Gomis-Rüth	xgrcri@ibmb.csic.es	IBMB-CSIC, Spain
Noa Martin Cofreces	noa.martin@salud.madrid.org	IIS La Princesa
María Llorens-Martin	mllorens@cbm.csic.es	CBM Severo Ochoa, Spain
Eduard Batlle	eduard.batlle@irbbarcelona.org	Institut de Recerca Biomèdica de Barcelona, IRB, Spain
Francesc Posas	Francesc.posas@irbbarcelona.org	Institut de Recerca Biomèdica de Barcelona, IRB, Spain
Javier deFelipe	defelipe@cajal.csic.es	CTB-UPM / Instituto Cajal, Spain
Fernando García Moreno	fernando.garcia-moreno@achucarro.org	Achucarro - Basque center for neuroscience, Spain
Joan Xavier Comella	joan.comella@sjd.es	Hospital Sant Joan de Déu de Barcelona, Spain
Bart Bijnens	bart@bijnens.com	Instituto de Investigaciones Biomédicas August Pi i Sunyer (IDIBAPS), Spain
Gustavo Egea	gegea@ub.edu	Instituto de Investigaciones Biomédicas August Pi i Sunyer (IDIBAPS), Spain
Olga Tura Ceide	otura@idibgi.org	Instituto de Investigación Biomedica Girona Josep Trueta (IDIBGI), Spain
Marga Nadal	mnadal@idibgi.org	Institut d'Investigació Biomèdica de Girona Josep Trueta (IDIBGI), Spain
Anne Bonnin	anne.bonnin@psi.ch	TOMCAT, SLS
Andreas Schaefer	andreas.schaefer@crick.ac.uk	The Francis Crick Institute, London, UK
Alberto Elorsegui Artola	alberto.eloseguiartola@crick.ac.uk	The Francis Crick Institute, London, UK
Nicoletta Petridou	nicoletta.petridou@embl.de	EMBL Barcelona
Hahn Vu	hanh.vu@embl.de	EMBL Barcelona
Ede Rancz	ede.rancz@inserm.fr	Institut de Neurobiologie de la Mediterraneé (INMED), Marseille, France
Hiram Castillo	hiram.castillo_michel@esrf.fr	ESRF, France
Alexandra Pacureanu	joitapac@esrf.fr	ESRF, France
Sylvain Bohic	bohic@esrf.fr	Inserm Unit UA7 & University grenoble Alpes, Grenoble, France
Pierre Legrand	pierre.legrand@synchrotron-soleil.fr	SOLEIL, France
Pierre Montaville	pierre.montaville@synchrotron-soleil.fr	SOLEIL, France
Christophe Chevalier	christophe.chevalier@inrae.fr	INRAe, France
Camille Rivard	camille.rivard@synchrotron-soleil.fr	INRAe, France
Richard Ortega	ortega@cenbg.in2p3.fr	CNRS, University of Bordeaux, France
Christopher Lefevre	Christopher.Lefevre@cea.fr	CEA Cadarache, France
Murielle Masi	muriel.masi@univ-amu.fr	INSERM, Aix-Marseille University, France
Karim Benzerara	karim.benzerara@sorbonne-universite.fr	Université de la Sorbone, France
Anastasia Gazi	anastasia.gazi@pasteur.fr	Institut Pasteur, France
Anna Sartori-Rupp	anna.sartori-rupp@pasteur.fr	Institut Pasteur, France
Celia Romao	cmromao@itqb.unl.pt	ITQV NOVA, Portugal
Leonard Chavas	l.chavas@nusr.nagoya-u.ac.jp	Nagoya University, Japan
Beatriz Guimaraes	beatriz.guimaraes@fiocruz.br	FIOCRUZ, Brasil
Sanna Sevanto	sanna@lanl.gov	Los Alamos National Laboratory, USA
Assaf Gal	assaf.gal@weizmann.ac.il	Weizmann Institute of Sciences, Israel
Stefano Iotti	stefano.iotti@unibo.it	University of Bologna (UNIBO), Italy

8. References

(1) Bleackley, M. R.; Macgillivray, R. T. Transition metal homeostasis: from yeast to human disease. *Biometals* **2011**, *24* (5), 785-809. DOI: 10.1007/s10534-011-9451-4.

(2) Kolaczkowska, E.; Kubes, P. Neutrophil recruitment and function in health and inflammation. *Nat Rev Immunol* **2013**, *13* (3), 159-175. DOI: 10.1038/nri3399.

(3) Niemiec, M. J.; De Samber, B.; Garrevoet, J.; Vergucht, E.; Vekemans, B.; De Rycke, R.; Björn, E.; Sandblad, L.; Wellenreuther, G.; Falkenberg, G.; et al. Trace element landscape of resting and activated human neutrophils on the sub-micrometer level. *Metallomics* **2015**, *7* (6), 996-1010. DOI: 10.1039/c4mt00346b.

(4) Grubaugh, N. D.; Ladner, J. T.; Lemey, P.; Pybus, O. G.; Rambaut, A.; Holmes, E. C.; Andersen, K. G. Tracking virus outbreaks in the twenty-first century. *Nat Microbiol* **2019**, *4* (1), 10-19. DOI: 10.1038/s41564-018-0296-2.

(5) Chasapis, C. T. Interactions between metal binding viral proteins and human targets as revealed by network-based bioinformatics. *J Inorg Biochem* **2018**, *186*, 157-161. DOI: 10.1016/j.jinorgbio.2018.06.012.

(6) Read, S. A.; O'Connor, K. S.; Suppiah, V.; Ahlenstiel, C. L. E.; Obeid, S.; Cook, K. M.; Cunningham, A.; Douglas, M. W.; Hogg, P. J.; Booth, D.; et al. Zinc is a potent and specific inhibitor of IFN-λ3 signalling. *Nat Commun* **2017**, *8*, 15245. DOI: 10.1038/ncomms15245.

(7) Liu, W.; Zhang, S.; Nekhai, S.; Liu, S. Depriving Iron Supply to the Virus Represents a Promising Adjuvant Therapeutic Against Viral Survival. *Curr Clin Microbiol Rep* **2020**, *7* (2), 13-19. DOI: 10.1007/s40588-020-00140-w.

(8) Maret, W. Zinc in Cellular Regulation: The Nature and Significance of "Zinc Signals". *Int J Mol Sci* **2017**, *18* (11). DOI: 10.3390/ijms18112285.

(9) Wessels, I.; Maywald, M.; Rink, L. Zinc as a Gatekeeper of Immune Function. *Nutrients* **2017**, *9* (12). DOI: 10.3390/nu9121286.

(10) Choi, R.; Kim, H. T.; Lim, Y.; Kim, M. J.; Kwon, O. J.; Jeon, K.; Park, H. Y.; Jeong, B. H.; Koh, W. J.; Lee, S. Y. Serum Concentrations of Trace Elements in Patients with Tuberculosis and Its Association with Treatment Outcome. *Nutrients* **2015**, *7* (7), 5969-5981. DOI: 10.3390/nu7075263.

(11) Kumar, A.; Kubota, Y.; Chernov, M.; Kasuya, H. Potential role of zinc supplementation in prophylaxis and treatment of COVID-19. *Med Hypotheses* **2020**, *144*, 109848. DOI: 10.1016/j.mehy.2020.109848.

(12) Cassat, J. E.; Skaar, E. P. Iron in infection and immunity. *Cell Host Microbe* **2013**, *13* (5), 509-519. DOI: 10.1016/j.chom.2013.04.010.

(13) Çam, H.; Yılmaz, N. Serum hepcidin levels are related to serum markers for iron metabolism and fibrosis stage in patients with chronic hepatitis B: A cross-sectional study. *Arab J Gastroenterol* **2020**, *21* (2), 85-90. DOI: 10.1016/j.ajg.2020.04.013.

(14) Weiss, G.; Carver, P. L. Role of divalent metals in infectious disease susceptibility and outcome. *Clin Microbiol Infect* **2018**, *24* (1), 16-23. DOI: 10.1016/j.cmi.2017.01.018.

(15) Raha, S.; Mallick, R.; Basak, S.; Duttaroy, A. K. Is copper beneficial for COVID-19 patients? *Med Hypotheses* **2020**, *142*, 109814. DOI: 10.1016/j.mehy.2020.109814.

(16) Antelo, G. T.; Vila, A. J.; Giedroc, D. P.; Capdevila, D. A. Molecular Evolution of Transition Metal Bioavailability at the Host-Pathogen Interface. *Trends Microbiol* **2021**, *29* (5), 441-457. DOI: 10.1016/j.tim.2020.08.001.

(17) Murdoch, C. C.; Skaar, E. P. Nutritional immunity: the battle for nutrient metals at the host-pathogen interface. *Nat Rev Microbiol* **2022**, *20* (11), 657-670. DOI: 10.1038/s41579-022-00745-6.

(18) Wagner, D.; Maser, J.; Lai, B.; Cai, Z.; Barry, C. E.; Höner Zu Bentrup, K.; Russell, D. G.; Bermudez, L. E. Elemental analysis of Mycobacterium avium-, Mycobacterium tuberculosis-, and Mycobacterium smegmatis-containing phagosomes indicates pathogen-induced microenvironments within the host cell's endosomal system. *J Immunol* **2005**, *174* (3), 1491-1500. DOI: 10.4049/jimmunol.174.3.1491.

(19) Venugopal, K.; Hentzschel, F.; Valkiūnas, G.; Marti, M. Plasmodium asexual growth and sexual development in the haematopoietic niche of the host. *Nat Rev Microbiol* **2020**, *18* (3), 177-189. DOI: 10.1038/s41579-019-0306-2.

(20) Kapishnikov, S.; Leiserowitz, L.; Yang, Y.; Cloetens, P.; Pereiro, E.; Awamu Ndonglack, F.; Matuschewski, K.; Als-Nielsen, J. Biochemistry of malaria parasite infected red blood cells by X-ray microscopy. *Sci Rep* **2017**, *7* (1), 802. DOI: 10.1038/s41598-017-00921-2.

(21) Frei, A.; Verderosa, A. D.; Elliott, A. G.; Zuegg, J.; Blaskovich, M. A. T. Metals to combat antimicrobial resistance. *Nat Rev Chem* **2023**, *7* (3), 202-224. DOI: 10.1038/s41570-023-00463-4.

(22) Kaščáková, S.; Maigre, L.; Chevalier, J.; Réfrégiers, M.; Pagès, J. M. Antibiotic transport in resistant bacteria: synchrotron UV fluorescence microscopy to determine antibiotic accumulation with single cell resolution. *PLoS One* **2012**, *7* (6), e38624. DOI: 10.1371/journal.pone.0038624.

(23) Cinquin, B.; Maigre, L.; Pinet, E.; Chevalier, J.; Stavenger, R. A.; Mills, S.; Réfrégiers, M.; Pagès, J. M. Microspectrometric insights on the uptake of antibiotics at the single bacterial cell level. *Sci Rep* **2015**, *5*, 17968. DOI: 10.1038/srep17968.

(24) Masi, M.; Dumont, E.; Vergalli, J.; Pajovic, J.; Réfrégiers, M.; Pagès, J. M. Fluorescence enlightens RND pump activity and the intrabacterial concentration of antibiotics. *Res Microbiol* **2018**, *169* (7-8), 432-441. DOI: 10.1016/j.resmic.2017.11.005.

(25) Vergalli, J.; Dumont, E.; Cinquin, B.; Maigre, L.; Pajovic, J.; Bacqué, E.; Mourez, M.; Réfrégiers, M.; Pagès, J. M. Fluoroquinolone structure and translocation flux across bacterial membrane. *Sci Rep* **2017**, *7* (1), 9821. DOI: 10.1038/s41598-017-08775-4.

(26) Vergalli, J.; Dumont, E.; Pajović, J.; Cinquin, B.; Maigre, L.; Masi, M.; Réfrégiers, M.; Pagés, J. M. Spectrofluorimetric quantification of antibiotic drug concentration in bacterial cells for the characterization of translocation across bacterial membranes. *Nat Protoc* **2018**, *13* (6), 1348-1361. DOI: 10.1038/nprot.2018.036.

(27) Dumont, E.; Vergalli, J.; Conraux, L.; Taillier, C.; Vassort, A.; Pajovic, J.; Réfrégiers, M.; Mourez, M.; Pagès, J. M. Antibiotics and efflux: combined spectrofluorimetry and mass spectrometry to evaluate the involvement of concentration and efflux activity in antibiotic intracellular accumulation. *J Antimicrob Chemother* **2019**, *74* (1), 58-65. DOI: 10.1093/jac/dky396.

(28) Vergalli, J.; Atzori, A.; Pajovic, J.; Dumont, E.; Malloci, G.; Masi, M.; Vargiu, A. V.; Winterhalter, M.; Réfrégiers, M.; Ruggerone, P.; et al. The challenge of intracellular antibiotic accumulation, a function of fluoroquinolone influx versus bacterial efflux. *Commun Biol* **2020**, *3* (1), 198. DOI: 10.1038/s42003-020-0929-x.

(29) Vergalli, J.; Chauvet, H.; Oliva, F.; Pajović, J.; Malloci, G.; Vargiu, A. V.; Réfrégiers, M.; Ruggerone, P.; Pagès, J. M. A framework for dissecting affinities of multidrug efflux transporter AcrB to fluoroquinolones. *Commun Biol* **2022**, *5* (1), 1062. DOI: 10.1038/s42003-022-04024-1.

(30) Ferreira, M.; Gameiro, P. Fluoroquinolone-Transition Metal Complexes: A Strategy to Overcome Bacterial Resistance. *Microorganisms* **2021**, *9* (7). DOI: 10.3390/microorganisms9071506.

(31) Conesa, J. J.; Carrasco, A. C.; Rodríguez-Fanjul, V.; Yang, Y.; Carrascosa, J. L.; Cloetens, P.; Pereiro, E.; Pizarro, A. M. Unambiguous Intracellular Localization and Quantification of a Potent Iridium Anticancer Compound by Correlative 3D Cryo X-Ray Imaging. *Angew Chem Int Ed Engl* **2020**, *59* (3), 1270-1278. DOI: 10.1002/anie.201911510.

(32) Harbort, C. J.; Hashimoto, M.; Inoue, H.; Niu, Y.; Guan, R.; Rombolà, A. D.; Kopriva, S.; Voges, M. J. E. E.; Sattely, E. S.; Garrido-Oter, R.; et al. Root-Secreted Coumarins and the Microbiota Interact to Improve Iron Nutrition in Arabidopsis. *Cell Host Microbe* **2020**, *28* (6), 825-837.e826. DOI: 10.1016/j.chom.2020.09.006.

(33) Stassen, M. J. J.; Hsu, S. H.; Pieterse, C. M. J.; Stringlis, I. A. Coumarin Communication Along the Microbiome-Root-Shoot Axis. *Trends Plant Sci* **2021**, *26* (2), 169-183. DOI: 10.1016/j.tplants.2020.09.008.

(34) Aznar, A.; Chen, N. W.; Thomine, S.; Dellagi, A. Immunity to plant pathogens and iron homeostasis. *Plant Sci* **2015**, *240*, 90-97. DOI: 10.1016/j.plantsci.2015.08.022.

(35) Escudero, V.; Ferreira Sánchez, D.; Abreu, I.; Sopeña-Torres, S.; Makarovsky-Saavedra, N.; Bernal, M.; Krämer, U.; Grolimund, D.; González-Guerrero, M.; Jordá, L. Arabidopsis thaliana Zn2+-efflux ATPases HMA2 and HMA4 are required for resistance to the necrotrophic fungus Plectosphaerella cucumerina BMM. *J Exp Bot* **2022**, *73* (1), 339-350. DOI: 10.1093/jxb/erab400.

(36) Hall-Stoodley, L.; Costerton, J. W.; Stoodley, P. Bacterial biofilms: from the natural environment to infectious diseases. *Nat Rev Microbiol* **2004**, *2* (2), 95-108. DOI: 10.1038/nrmicro821.

(37) Bari, A. K.; Belalekar, T. S.; Poojary, A.; Rohra, S. Combination drug strategies for biofilm eradication using synthetic and natural agents in KAPE pathogens. *Front Cell Infect Microbiol* **2023**, *13*, 1155699. DOI: 10.3389/fcimb.2023.1155699.

(38) Salvati, A.; Pitek, A. S.; Monopoli, M. P.; Prapainop, K.; Bombelli, F. B.; Hristov, D. R.; Kelly, P. M.; Åberg, C.; Mahon, E.; Dawson, K. A. Transferrin-functionalized nanoparticles lose their targeting capabilities when a biomolecule corona adsorbs on the surface. *Nat Nanotechnol* **2013**, *8* (2), 137-143. DOI: 10.1038/nnano.2012.237.

(39) Feliu, N.; Docter, D.; Heine, M.; Del Pino, P.; Ashraf, S.; Kolosnjaj-Tabi, J.; Macchiarini, P.; Nielsen, P.; Alloyeau, D.; Gazeau, F.; et al. In vivo degeneration and the fate of inorganic nanoparticles. *Chem Soc Rev* **2016**, *45* (9), 2440-2457. DOI: 10.1039/c5cs00699f.

(40) Veronesi, G.; Deniaud, A.; Gallon, T.; Jouneau, P. H.; Villanova, J.; Delangle, P.; Carrière, M.; Kieffer, I.; Charbonnier, P.; Mintz, E.; et al. Visualization, quantification and coordination of Ag. *Nanoscale* **2016**, *8* (38), 17012-17021. DOI: 10.1039/c6nr04381j.

(41) Veronesi, G.; Aude-Garcia, C.; Kieffer, I.; Gallon, T.; Delangle, P.; Herlin-Boime, N.; Rabilloud, T.; Carrière, M. Exposure-dependent Ag+ release from silver nanoparticles and its complexation in AgS2 sites in primary murine macrophages. *Nanoscale* **2015**, *7* (16), 7323-7330. DOI: 10.1039/c5nr00353a.

(42) Lehmann, S. G.; Toybou, D.; Pradas Del Real, A. E.; Arndt, D.; Tagmount, A.; Viau, M.; Safi, M.; Pacureanu, A.; Cloetens, P.; Bohic, S.; et al. Crumpling of silver nanowires by endolysosomes strongly reduces toxicity. *Proc Natl Acad Sci U S A* **2019**, *116* (30), 14893-14898. DOI: 10.1073/pnas.1820041116.

(43) Yuan, Y.; Chen, S.; Paunesku, T.; Gleber, S. C.; Liu, W. C.; Doty, C. B.; Mak, R.; Deng, J.; Jin, Q.; Lai, B.; et al. Epidermal growth factor receptor targeted nuclear delivery and high-resolution whole cell X-ray imaging of Fe3O4@TiO2 nanoparticles in cancer cells. *ACS Nano* **2013**, *7* (12), 10502-10517. DOI: 10.1021/nn4033294.

(44) Vitol, E. A.; Rozhkova, E. A.; Rose, V.; Stripe, B. D.; Young, N. R.; Cohen, E. E. W.; Leoni, L.; Novosad, V. Efficient Cisplatin Pro-Drug Delivery Visualized with Sub-100 nm Resolution: Interfacing Engineered Thermosensitive Magnetomicelles with a Living System. *Advanced Materials Interfaces* **2014**, *1* (7), 1400182. DOI: https://doi.org/10.1002/admi.201400182.

(45) Curcio, A.; Van de Walle, A.; Serrano, A.; Preveral, S.; Péchoux, C.; Pignol, D.; Menguy, N.; Lefevre, C. T.; Espinosa, A.; Wilhelm, C. Transformation Cycle of Magnetosomes in Human Stem Cells: From Degradation to Biosynthesis of Magnetic Nanoparticles Anew. *ACS Nano* **2020**, *14* (2), 1406-1417. DOI: 10.1021/acsnano.9b08061.

(46) Curcio, A.; de Walle, A. V.; Benassai, E.; Serrano, A.; Luciani, N.; Menguy, N.; Manshian, B. B.; Sargsian, A.; Soenen, S.; Espinosa, A.; et al. Massive Intracellular Remodeling of CuS Nanomaterials Produces Nontoxic Bioengineered Structures with Preserved Photothermal Potential. *ACS Nano* **2021**, *15* (6), 9782-9795. DOI: 10.1021/acsnano.1c00567.

(47) Wang, L.; Zhang, T.; Li, P.; Huang, W.; Tang, J.; Wang, P.; Liu, J.; Yuan, Q.; Bai, R.; Li, B.; et al. Use of Synchrotron Radiation-Analytical Techniques To Reveal Chemical Origin of Silver-Nanoparticle Cytotoxicity. *ACS Nano* **2015**, *9* (6), 6532-6547. DOI: 10.1021/acsnano.5b02483.

(48) Mei, L.; Zhang, X.; Yin, W.; Dong, X.; Guo, Z.; Fu, W.; Su, C.; Gu, Z.; Zhao, Y. Translocation, biotransformation-related degradation, and toxicity assessment of polyvinylpyrrolidone-modified 2H-phase nano-MoS. *Nanoscale* **2019**, *11* (11), 4767-4780. DOI: 10.1039/c8nr10319d.

(49) Tomás-Gamasa, M.; Martínez-Calvo, M.; Couceiro, J. R.; Mascareñas, J. L. Transition metal catalysis in the mitochondria of living cells. *Nat Commun* **2016**, *7*, 12538. DOI: 10.1038/ncomms12538.

(50) Miguel-Ávila, J.; Tomás-Gamasa, M.; Mascareñas, J. L. Intracellular Ruthenium-Promoted (2+2+2) Cycloadditions. *Angew Chem Int Ed Engl* **2020**, *59* (40), 17628-17633. DOI: 10.1002/anie.202006689.

(51) Uttamapinant, C.; Tangpeerachaikul, A.; Grecian, S.; Clarke, S.; Singh, U.; Slade, P.; Gee, K. R.; Ting, A. Y. Fast, cell-compatible click chemistry with copper-chelating azides for biomolecular labeling. *Angew Chem Int Ed Engl* **2012**, *51* (24), 5852-5856. DOI: 10.1002/anie.201108181.

(52) Pérez-López, A. M.; Rubio-Ruiz, B.; Sebastián, V.; Hamilton, L.; Adam, C.; Bray, T. L.; Irusta, S.; Brennan, P. M.; Lloyd-Jones, G. C.; Sieger, D.; et al. Gold-Triggered Uncaging Chemistry in Living Systems. *Angew Chem Int Ed Engl* **2017**, *56* (41), 12548-12552. DOI: 10.1002/anie.201705609.

(53) Sasmal, P. K.; Carregal-Romero, S.; Han, A. A.; Streu, C. N.; Lin, Z.; Namikawa, K.; Elliott, S. L.; Köster, R. W.; Parak, W. J.; Meggers, E. Catalytic azide reduction in biological environments. *Chembiochem* **2012**, *13* (8), 1116-1120. DOI: 10.1002/cbic.201100719.

(54) Madec, H.; Figueiredo, F.; Cariou, K.; Roland, S.; Sollogoub, M.; Gasser, G. Metal complexes for catalytic and photocatalytic reactions in living cells and organisms. *Chem Sci* **2023**, *14* (3), 409-442. DOI: 10.1039/d2sc05672k.

(55) Soldevila-Barreda, J. J.; Metzler-Nolte, N. Intracellular Catalysis with Selected Metal Complexes and Metallic Nanoparticles: Advances toward the Development of Catalytic Metallodrugs. *Chem Rev* **2019**, *119* (2), 829-869. DOI: 10.1021/acs.chemrev.8b00493.

(56) Martínez-Calvo, M.; Mascareñas, J. L. Organometallic catalysis in biological media and living settings. *Coordination Chemistry Reviews* **2018**, *359*, 57-79. DOI: https://doi.org/10.1016/j.ccr.2018.01.011.

(57) Bai, Y.; Chen, J.; Zimmerman, S. C. Designed transition metal catalysts for intracellular organic synthesis. *Chem Soc Rev* **2018**, *47* (5), 1811-1821. DOI: 10.1039/c7cs00447h.

(58) Ngo, A. H.; Bose, S.; Do, L. H. Intracellular Chemistry: Integrating Molecular Inorganic Catalysts with Living Systems. *Chemistry* **2018**, *24* (42), 10584-10594. DOI: 10.1002/chem.201800504.

(59) Vidal, C.; Tomás-Gamasa, M.; Gutiérrez-González, A.; Mascareñas, J. L. Ruthenium-Catalyzed Redox Isomerizations inside Living Cells. *J Am Chem Soc* **2019**, *141* (13), 5125-5129. DOI: 10.1021/jacs.9b00837.

(60) Coverdale, J. P. C.; Romero-Canelón, I.; Sanchez-Cano, C.; Clarkson, G. J.; Habtemariam, A.; Wills, M.; Sadler, P. J. Asymmetric transfer hydrogenation by synthetic catalysts in cancer cells. *Nat Chem* **2018**, *10* (3), 347-354. DOI: 10.1038/nchem.2918.

(61) Crabtree, R. H. Deactivation in homogeneous transition metal catalysis: causes, avoidance, and cure. *Chem Rev* **2015**, *115* (1), 127-150. DOI: 10.1021/cr5004375.

(62) Bolitho, E. M.; Coverdale, J. P. C.; Bridgewater, H. E.; Clarkson, G. J.; Quinn, P. D.; Sanchez-Cano, C.; Sadler, P. J. Tracking Reactions of Asymmetric Organo-Osmium Transfer Hydrogenation Catalysts in Cancer Cells. *Angew Chem Int Ed Engl* **2021**, *60* (12), 6462-6472. DOI: 10.1002/anie.202016456.

(63) Bolitho, E. M.; Bridgewater, H. E.; Needham, R. J.; Coverdale, J. P. C.; Quinn, P. D.; Sanchez-Cano, C.; Sadler, P. J. Elemental mapping of half-sandwich azopyridine osmium arene complexes in cancer cells. *Inorganic Chemistry Frontiers* **2021**, *8* (15), 3675-3685, 10.1039/D1QI00512J. DOI: 10.1039/D1QI00512J.

(64) James, S. A.; Burke, R.; Howard, D. L.; Spiers, K. M.; Paterson, D. J.; Murphy, S.; Ramm, G.; Kirkham, R.; Ryan, C. G.; de Jonge, M. D. Visualising coordination chemistry: fluorescence X-ray absorption near edge structure tomography. *Chem Commun (Camb)* **2016**, *52* (79), 11834-11837. DOI: 10.1039/c6cc06747f.

(65) James, S. A.; Hare, D. J.; Jenkins, N. L.; de Jonge, M. D.; Bush, A. I.; McColl, G. φXANES: In vivo imaging of metal-protein coordination environments. *Sci Rep* **2016**, *6*, 20350. DOI: 10.1038/srep20350.

(66) Wu, L. E.; Levina, A.; Harris, H. H.; Cai, Z.; Lai, B.; Vogt, S.; James, D. E.; Lay, P. A. Carcinogenic Chromium(VI) Compounds Formed by Intracellular Oxidation of Chromium(III) Dietary Supplements by Adipocytes. *Angew Chem Int Ed Engl* **2016**, *55* (5), 1742-1745. DOI: 10.1002/anie.201509065.

(67) Sanchez-Cano, C.; Gianolio, D.; Romero-Canelon, I.; Tucoulou, R.; Sadler, P. J. Nanofocused synchrotron X-ray absorption studies of the intracellular redox state of an organometallic complex in cancer cells. *Chem Commun (Camb)* **2019**, *55* (49), 7065-7068. DOI: 10.1039/c9cc01675a.

(68) Bolitho, E. M.; Sanchez-Cano, C.; Shi, H.; Quinn, P. D.; Harkiolaki, M.; Imberti, C.; Sadler, P. J. Single-Cell Chemistry of Photoactivatable Platinum Anticancer Complexes. *J Am Chem Soc* **2021**, *143* (48), 20224-20240. DOI: 10.1021/jacs.1c08630.

(69) Pattammattel, A.; Tappero, R.; Gavrilov, D.; Zhang, H.; Aronstein, P.; Forman, H. J.; O'Day, P. A.; Yan, H.; Chu, Y. S. Multimodal X-ray nano-spectromicroscopy analysis of chemically heterogeneous systems. *Metallomics* **2022**, *14* (10). DOI: 10.1093/mtomcs/mfac078.

(70) Kempner, E. S.; Wood, R.; Salovey, R. The temperature dependence of radiation sensitivity of large molecules. *Journal of Polymer Science Part B: Polymer Physics* **1986**, *24* (10), 2337-2343, https://doi.org/10.1002/polb.1986.090241015. DOI: https://doi.org/10.1002/polb.1986.090241015 (acccessed 2023/05/16).

(71) Hope, H. Crystallography of biological macromolecules at ultra-low temperature. *Annu Rev Biophys Biophys Chem* **1990**, *19*, 107-126. DOI: 10.1146/annurev.bb.19.060190.000543.

(72) Heal, M. R.; Kumar, P.; Harrison, R. M. Particles, air quality, policy and health. *Chemical Society Reviews* **2012**, *41* (19), 6606-6630, 10.1039/C2CS35076A. DOI: 10.1039/C2CS35076A.

(73) Murr, L. E.; Garza, K. M. Natural and anthropogenic environmental nanoparticulates: Their microstructural characterization and respiratory health implications. *Atmospheric Environment* **2009**, *43*, 2683-2692.

(74) Braakhuis, H. M.; Park, M. V. D. Z.; Gosens, I.; De Jong, W. H.; Cassee, F. R. Physicochemical characteristics of nanomaterials that affect pulmonary inflammation. *Particle and Fibre Toxicology* **2014**, *11* (1), 18. DOI: 10.1186/1743-8977-11-18.

(75) Bakand, S.; Hayes, A.; Dechsakulthorn, F. Nanoparticles: a review of particle toxicology following inhalation exposure. *Inhal Toxicol* **2012**, *24* (2), 125-135. DOI: 10.3109/08958378.2010.642021 From NLM.

(76) Alam, M. S.; Zeraati-Rezaei, S.; Stark, C. P.; Liang, Z.; Xu, H.; Harrison, R. M. The characterisation of diesel exhaust particles – composition, size distribution and partitioning. *Faraday Discussions* **2016**, *189* (0), 69-84, 10.1039/C5FD00185D. DOI: 10.1039/C5FD00185D.

(77) Sanderson, P.; Delgado-Saborit, J. M.; Harrison, R. M. A review of chemical and physical characterisation of atmospheric metallic nanoparticles. *Atmospheric Environment* **2014**, *94*, 353-365. DOI: https://doi.org/10.1016/j.atmosenv.2014.05.023.

(78) Maurer-Jones, M. A.; Gunsolus, I. L.; Murphy, C. J.; Haynes, C. L. Toxicity of engineered nanoparticles in the environment. *Anal Chem* **2013**, *85* (6), 3036-3049. DOI: 10.1021/ac303636s.

(79) Mueller, N. C.; Nowack, B. Exposure Modeling of Engineered Nanoparticles in the Environment. *Environmental Science & Technology* **2008**, *42* (12), 4447-4453. DOI: 10.1021/es7029637.

(80) Shelley, M. L.; Wagner, A. J.; Hussain, S. M.; Bleckmann, C. Modeling the in vivo case with in vitro nanotoxicity data. *Int J Toxicol* **2008**, *27* (5), 359-367. DOI: 10.1080/10915810802503487 From NLM.

(81) Triboulet, S.; Aude-Garcia, C.; Armand, L.; Gerdil, A.; Diemer, H.; Proamer, F.; Collin-Faure, V.; Habert, A.; Strub, J.-M.; Hanau, D.; et al. Analysis of cellular responses of macrophages to zinc ions and zinc oxide nanoparticles: a combined targeted and proteomic approach. *Nanoscale* **2014**, *6* (11), 6102-6114, 10.1039/C4NR00319E. DOI: 10.1039/C4NR00319E.

(82) Limbach, L. K.; Wick, P.; Manser, P.; Grass, R. N.; Bruinink, A.; Stark, W. J. Exposure of Engineered Nanoparticles to Human Lung Epithelial Cells: Influence of Chemical Composition and Catalytic Activity

on Oxidative Stress. *Environmental Science & Technology* **2007**, *41* (11), 4158-4163. DOI: 10.1021/es062629t.

(83) Karlsson, H. L.; Cronholm, P.; Gustafsson, J.; Möller, L. Copper oxide nanoparticles are highly toxic: a comparison between metal oxide nanoparticles and carbon nanotubes. *Chem Res Toxicol* **2008**, *21* (9), 1726-1732. DOI: 10.1021/tx800064j From NLM.

(84) Magaye, R.; Zhao, J.; Bowman, L.; Ding, M. Genotoxicity and carcinogenicity of cobalt-, nickel- and copper-based nanoparticles. In *Exp Ther Med*, Vol. 4; 2012; pp 551-561.

(85) Nel, A.; Xia, T.; Mädler, L.; Li, N. Toxic potential of materials at the nanolevel. *Science* **2006**, *311* (5761), 622-627. DOI: 10.1126/science.1114397 From NLM.

(86) Magaye, R.; Zhou, Q.; Bowman, L.; Zou, B.; Mao, G.; Xu, J.; Castranova, V.; Zhao, J.; Ding, M. Metallic nickel nanoparticles may exhibit higher carcinogenic potential than fine particles in JB6 cells. *PLoS One* **2014**, *9* (4), e92418. DOI: 10.1371/journal.pone.0092418 From NLM.

(87) Gliga, A. R.; Skoglund, S.; Odnevall Wallinder, I.; Fadeel, B.; Karlsson, H. L. Size-dependent cytotoxicity of silver nanoparticles in human lung cells: the role of cellular uptake, agglomeration and Ag release. *Particle and Fibre Toxicology* **2014**, *11* (1), 11. DOI: 10.1186/1743-8977-11-11.

(88) Chevallet, M.; Veronesi, G.; Fuchs, A.; Mintz, E.; Michaud-Soret, I.; Deniaud, A. Impact of labile metal nanoparticles on cellular homeostasis. Current developments in imaging, synthesis and applications. *Biochim Biophys Acta Gen Subj* **2017**, *1861* (6), 1566-1577. DOI: 10.1016/j.bbagen.2016.12.012 From NLM.

(89) Wang, Z.; Liu, S.; Ma, J.; Qu, G.; Wang, X.; Yu, S.; He, J.; Liu, J.; Xia, T.; Jiang, G.-B. Silver Nanoparticles Induced RNA Polymerase-Silver Binding and RNA Transcription Inhibition in Erythroid Progenitor Cells. *ACS Nano* **2013**, *7* (5), 4171-4186. DOI: 10.1021/nn400594s.

(90) Boulanger, G.; Andujar, P.; Pairon, J. C.; Billon-Galland, M. A.; Dion, C.; Dumortier, P.; Brochard, P.; Sobaszek, A.; Bartsch, P.; Paris, C.; et al. Quantification of short and long asbestos fibers to assess asbestos exposure: a review of fiber size toxicity. *Environ Health* **2014**, *13*, 59. DOI: 10.1186/1476-069X-13-59.

(91) Gualtieri, A. F.; Bursi Gandolfi, N.; Pollastri, S.; Burghammer, M.; Tibaldi, E.; Belpoggi, F.; Pollok, K.; Langenhorst, F.; Vigliaturo, R.; Dražić, G. New insights into the toxicity of mineral fibres: A combined in situ synchrotron μ-XRD and HR-TEM study of chrysotile, crocidolite, and erionite fibres found in the tissues of Sprague-Dawley rats. *Toxicol Lett* **2017**, *274*, 20-30. DOI: 10.1016/j.toxlet.2017.04.004.

(92) Gianoncelli, A.; Kourousias, G.; Pascolo, L.; Rizzardi, C.; Ceccone, G.; Kaulich, B.; Kiskinova, M. Life science applications and research potential of the TwinMic spectromicroscopy station at ELETTRA. *Journal of Physics: Conference Series* **2013**, *463* (1), 012004. DOI: 10.1088/1742-6596/463/1/012004.

(93) Bardelli, F.; Veronesi, G.; Capella, S.; Bellis, D.; Charlet, L.; Cedola, A.; Belluso, E. New insights on the biomineralisation process developing in human lungs around inhaled asbestos fibres. *Sci Rep* **2017**, *7*, 44862. DOI: 10.1038/srep44862.

(94) Bardelli, F.; Brun, F.; De Panfilis, S.; Cloetens, P.; Capella, S.; Belluso, E.; Bellis, D.; Di Napoli, A.; Cedola, A. Chemo-physical properties of asbestos bodies in human lung tissues studied at the nano-scale by non-invasive, label free x-ray imaging and spectroscopic techniques. *Toxicol Lett* **2021**, *348*, 18-27. DOI: 10.1016/j.toxlet.2021.05.002.

(95) Cloetens, P.; Ludwig, W.; Baruchel, J.; Van Dyck, D.; Van Landuyt, J.; Guigay, J. P.; Schlenker, M. Holotomography: Quantitative phase tomography with micrometer resolution using hard synchrotron radiation x rays. *Applied Physics Letters* **1999**, *75* (19), 2912-2914. DOI: 10.1063/1.125225 (acccessed 5/16/2023).

(96) Massimi, L.; Bukreeva, I.; Santamaria, G.; Fratini, M.; Corbelli, A.; Brun, F.; Fumagalli, S.; Maugeri, L.; Pacureanu, A.; Cloetens, P.; et al. Exploring Alzheimer's disease mouse brain through X-ray phase contrast tomography: From the cell to the organ. *Neuroimage* **2019**, *184*, 490-495. DOI: 10.1016/j.neuroimage.2018.09.044.

(97) Cedola, A.; Bravin, A.; Bukreeva, I.; Fratini, M.; Pacureanu, A.; Mittone, A.; Massimi, L.; Cloetens, P.; Coan, P.; Campi, G.; et al. X-Ray Phase Contrast Tomography Reveals Early Vascular Alterations and Neuronal Loss in a Multiple Sclerosis Model. *Sci Rep* **2017**, *7* (1), 5890. DOI: 10.1038/s41598-017-06251-7.

(98) Kuan, A. T.; Phelps, J. S.; Thomas, L. A.; Nguyen, T. M.; Han, J.; Chen, C. L.; Azevedo, A. W.; Tuthill, J. C.; Funke, J.; Cloetens, P.; et al. Dense neuronal reconstruction through X-ray holographic nano-tomography. *Nat Neurosci* **2020**, *23* (12), 1637-1643. DOI: 10.1038/s41593-020-0704-9.

(99) Wittig, N. K.; Laugesen, M.; Birkbak, M. E.; Bach-Gansmo, F. L.; Pacureanu, A.; Bruns, S.; Wendelboe, M. H.; Brüel, A.; Sørensen, H. O.; Thomsen, J. S.; et al. Canalicular Junctions in the Osteocyte Lacuno-Canalicular Network of Cortical Bone. *ACS Nano* **2019**, *13* (6), 6421-6430. DOI: 10.1021/acsnano.8b08478.

(100) Yu, B.; Pacureanu, A.; Olivier, C.; Cloetens, P.; Peyrin, F. Assessment of the human bone lacuno-canalicular network at the nanoscale and impact of spatial resolution. *Sci Rep* **2020**, *10* (1), 4567. DOI: 10.1038/s41598-020-61269-8.

(101) López-Guimet, J.; Peña-Pérez, L.; Bradley, R. S.; García-Canadilla, P.; Disney, C.; Geng, H.; Bodey, A. J.; Withers, P. J.; Bijnens, B.; Sherratt, M. J. MicroCT imaging reveals differential 3D micro-scale remodelling of the murine aorta in ageing and Marfan syndrome. *Theranostics* **2018**, *8* (21), 6038.

(102) Barbone, G. E.; Bravin, A.; Mittone, A.; Pacureanu, A.; Mascio, G.; Di Pietro, P.; Kraiger, M. J.; Eckermann, M.; Romano, M.; Hrabě de Angelis, M.; et al. X-ray multiscale 3D neuroimaging to quantify cellular aging and neurodegeneration postmortem in a model of Alzheimer's disease. *Eur J Nucl Med Mol Imaging* **2022**, *49* (13), 4338-4357. DOI: 10.1007/s00259-022-05896-5.

(103) Winding, M.; Pedigo, B. D.; Barnes, C. L.; Patsolic, H. G.; Park, Y.; Kazimiers, T.; Fushiki, A.; Andrade, I. V.; Khandelwal, A.; Valdes-Aleman, J.; et al. The connectome of an insect brain. *Science* **2023**, *379* (6636), eadd9330. DOI: 10.1126/science.add9330.

(104) White, J. G.; Southgate, E.; Thomson, J. N.; Brenner, S. The structure of the nervous system of the nematode Caenorhabditis elegans. *Philos Trans R Soc Lond B Biol Sci* **1986**, *314* (1165), 1-340. DOI: 10.1098/rstb.1986.0056.

(105) Helmstaedter, M. Cellular-resolution connectomics: challenges of dense neural circuit reconstruction. *Nat Methods* **2013**, *10* (6), 501-507. DOI: 10.1038/nmeth.2476.

(106) Abbott, L. F.; Bock, D. D.; Callaway, E. M.; Denk, W.; Dulac, C.; Fairhall, A. L.; Fiete, I.; Harris, K. M.; Helmstaedter, M.; Jain, V.; et al. The Mind of a Mouse. *Cell* **2020**, *182* (6), 1372-1376. DOI: 10.1016/j.cell.2020.08.010.

(107) Kornfeld, J.; Denk, W. Progress and remaining challenges in high-throughput volume electron microscopy. *Curr Opin Neurobiol* **2018**, *50*, 261-267. DOI: 10.1016/j.conb.2018.04.030.

(108) Briggman, K. L.; Helmstaedter, M.; Denk, W. Wiring specificity in the direction-selectivity circuit of the retina. *Nature* **2011**, *471* (7337), 183-188. DOI: 10.1038/nature09818.

(109) Bosch, C.; Ackels, T.; Pacureanu, A.; Zhang, Y.; Peddie, C. J.; Berning, M.; Rzepka, N.; Zdora, M. C.; Whiteley, I.; Storm, M.; et al. Functional and multiscale 3D structural investigation of brain tissue through correlative in vivo physiology, synchrotron microtomography and volume electron microscopy. *Nat Commun* **2022**, *13* (1), 2923. DOI: 10.1038/s41467-022-30199-6.

(110) Bortel, E.; Grover, L. M.; Eisenstein, N.; Seim, C.; Suhonen, H.; Pacureanu, A.; Westenberger, P.; Raum, K.; Langer, M.; Peyrin, F.; et al. Interconnectivity Explains High Canalicular Network Robustness between Neighboring Osteocyte Lacunae in Human Bone. *Advanced NanoBiomed Research* **2022**, *2* (4), 2100090, https://doi.org/10.1002/anbr.202100090. DOI: https://doi.org/10.1002/anbr.202100090 (acccessed 2023/05/16).

(111) Yu, B.; Pacureanu, A.; Olivier, C.; Cloetens, P.; Peyrin, F. Quantification of the bone lacunocanalicular network from 3D X-ray phase nanotomography images. *J Microsc* **2021**, *282* (1), 30-44. DOI: 10.1111/jmi.12973.

(112) Lowenstam, H. A.; Weiner, S. *On Biomineralization*; Oxford University Press, 1989. DOI: 10.1093/oso/9780195049770.001.0001.

(113) Beniash, E. Biominerals--hierarchical nanocomposites: the example of bone. *Wiley Interdiscip Rev Nanomed Nanobiotechnol* **2011**, *3* (1), 47-69. DOI: 10.1002/wnan.105.

(114) Deng, Z.; Jia, Z.; Li, L. Biomineralized Materials as Model Systems for Structural Composites: Intracrystalline Structural Features and Their Strengthening and Toughening Mechanisms. *Adv Sci (Weinh)* **2022**, *9* (14), e2103524. DOI: 10.1002/advs.202103524.

(115) Kirschvink, J. L.; Kobayashi-Kirschvink, A.; Woodford, B. J. Magnetite biomineralization in the human brain. *Proceedings of the National Academy of Sciences* **1992**, *89* (16), 7683-7687.

(116) Roy, D. M.; Linnehan, S. K. Hydroxyapatite formed from coral skeletal carbonate by hydrothermal exchange. *Nature* **1974**, *247* (5438), 220-222. DOI: 10.1038/247220a0.

(117) Ohira, T.; Ishikawa, K.; Kumamoto, S. H. I. Hydroxyapatite deposition in articular cartilage by intra-articular injections of methylprednisolone: a histological, ultrastructural, and X-ray-microprobe analysis in rabbits. *Journal of bone and joint surgery. American volume* **1986**, *68* (4), 509-520. From Inist-CNRS PASCAL.

(118) Kular, J.; Tickner, J.; Chim, S. M.; Xu, J. An overview of the regulation of bone remodelling at the cellular level. *Clin Biochem* **2012**, *45* (12), 863-873. DOI: 10.1016/j.clinbiochem.2012.03.021.

(119) Longhi, A.; Errani, C.; De Paolis, M.; Mercuri, M.; Bacci, G. Primary bone osteosarcoma in the pediatric age: state of the art. *Cancer Treat Rev* **2006**, *32* (6), 423-436. DOI: 10.1016/j.ctrv.2006.05.005.

(120) Allison, D. C.; Carney, S. C.; Ahlmann, E. R.; Hendifar, A.; Chawla, S.; Fedenko, A.; Angeles, C.; Menendez, L. R. A meta-analysis of osteosarcoma outcomes in the modern medical era. *Sarcoma* **2012**, *2012*, 704872. DOI: 10.1155/2012/704872.

(121) Weiner, S.; Wagner, H. D. THE MATERIAL BONE: Structure-Mechanical Function Relations. *Annual Review of Materials Science* **1998**, *28*, 271-298.

(122) Procopio, A.; Malucelli, E.; Pacureanu, A.; Cappadone, C.; Farruggia, G.; Sargenti, A.; Castiglioni, S.; Altamura, D.; Sorrentino, A.; Giannini, C.; et al. Chemical Fingerprint of Zn-Hydroxyapatite in the Early Stages of Osteogenic Differentiation. *ACS Cent Sci* **2019**, *5* (8), 1449-1460. DOI: 10.1021/acscentsci.9b00509.

(123) Sorrentino, A.; Malucelli, E.; Rossi, F.; Cappadone, C.; Farruggia, G.; Moscheni, C.; Perez-Berna, A. J.; Conesa, J. J.; Colletti, C.; Roveri, N.; et al. Calcite as a Precursor of Hydroxyapatite in the Early Biomineralization of Differentiating Human Bone-Marrow Mesenchymal Stem Cells. *Int J Mol Sci* **2021**, *22* (9). DOI: 10.3390/ijms22094939.

(124) Ziveri, P.; de Bernardi, B.; Baumann, K.-H.; Stoll, H. M.; Mortyn, P. G. Sinking of coccolith carbonate and potential contribution to organic carbon ballasting in the deep ocean. *Deep Sea Research Part II: Topical Studies in Oceanography* **2007**, *54* (5), 659-675. DOI: https://doi.org/10.1016/j.dsr2.2007.01.006.

(125) Kahil, K.; Weiner, S.; Addadi, L.; Gal, A. Ion Pathways in Biomineralization: Perspectives on Uptake, Transport, and Deposition of Calcium, Carbonate, and Phosphate. *J Am Chem Soc* **2021**, *143* (50), 21100-21112. DOI: 10.1021/jacs.1c09174.

(126) Milliman, J. D. Production and accumulation of calcium carbonate in the ocean: Budget of a nonsteady state. *Global Biogeochemical Cycles* **1993**, *7* (4), 927-957, https://doi.org/10.1029/93GB02524. DOI: https://doi.org/10.1029/93GB02524 (acccessed 2023/05/16).

(127) Sviben, S.; Gal, A.; Hood, M. A.; Bertinetti, L.; Politi, Y.; Bennet, M.; Krishnamoorthy, P.; Schertel, A.; Wirth, R.; Sorrentino, A.; et al. A vacuole-like compartment concentrates a disordered calcium phase in a key coccolithophorid alga. *Nat Commun* **2016**, *7*, 11228. DOI: 10.1038/ncomms11228.

(128) Gal, A.; Sviben, S.; Wirth, R.; Schreiber, A.; Lassalle-Kaiser, B.; Faivre, D.; Scheffel, A. Trace-Element Incorporation into Intracellular Pools Uncovers Calcium-Pathways in a Coccolithophore. *Adv Sci (Weinh)* **2017**, *4* (10), 1700088. DOI: 10.1002/advs.201700088.

(129) Kadan, Y.; Tollervey, F.; Varsano, N.; Mahamid, J.; Gal, A. Intracellular nanoscale architecture as a master regulator of calcium carbonate crystallization in marine microalgae. *Proc Natl Acad Sci U S A* **2021**, *118* (46). DOI: 10.1073/pnas.2025670118.

(130) Monteil, C. L.; Benzerara, K.; Menguy, N.; Bidaud, C. C.; Michot-Achdjian, E.; Bolzoni, R.; Mathon, F. P.; Coutaud, M.; Alonso, B.; Garau, C.; et al. Intracellular amorphous Ca-carbonate and magnetite biomineralization by a magnetotactic bacterium affiliated to the Alphaproteobacteria. *The ISME Journal* **2021**, *15* (1), 1-18. DOI: 10.1038/s41396-020-00747-3.

(131) Couradeau, E.; Benzerara, K.; Gérard, E.; Moreira, D.; Bernard, S.; Brown, G. E.; López-García, P. An early-branching microbialite cyanobacterium forms intracellular carbonates. *Science* **2012**, *336* (6080), 459-462. DOI: 10.1126/science.1216171.

(132) Segovia-Campos, I.; Martignier, A.; Filella, M.; Jaquet, J. M.; Ariztegui, D. Micropearls and other intracellular inclusions of amorphous calcium carbonate: an unsuspected biomineralization capacity shared by diverse microorganisms. *Environ Microbiol* **2022**, *24* (2), 537-550. DOI: 10.1111/1462-2920.15498 From NLM.

(133) Choudhary, S.; Sar, P. Uranium biomineralization by a metal resistant Pseudomonas aeruginosa strain isolated from contaminated mine waste. *Journal of Hazardous Materials* **2011**, *186* (1), 336-343. DOI: https://doi.org/10.1016/j.jhazmat.2010.11.004.

(134) Watanabe, K. Microorganisms relevant to bioremediation. *Current Opinion in Biotechnology* **2001**, *12* (3), 237-241. DOI: https://doi.org/10.1016/S0958-1669(00)00205-6.

(135) Gadd, G. M. Metals, minerals and microbes: geomicrobiology and bioremediation. *Microbiology (Reading)* **2010**, *156* (Pt 3), 609-643. DOI: 10.1099/mic.0.037143-0.

(136) Park, Y.; Eyal, Z.; Pekker, P.; Chevrier, D. M.; Lefèvre, C. T.; Arnoux, P.; Armengaud, J.; Monteil, C. L.; Gal, A.; Pósfai, M.; et al. Periplasmic Bacterial Biomineralization of Copper Sulfide Nanoparticles. *Advanced Science* **2022**, *9* (28), 2203444, https://doi.org/10.1002/advs.202203444. DOI: https://doi.org/10.1002/advs.202203444 (acccessed 2023/05/16).

(137) Chevrier, D. M.; Cerdá-Doñate, E.; Park, Y.; Cacho-Nerin, F.; Gomez-Gonzalez, M.; Uebe, R.; Faivre, D. Synchrotron-Based Nano-X-Ray Absorption Near-Edge Structure Revealing Intracellular Heterogeneity of Iron Species in Magnetotactic Bacteria. *Small Science* **2022**, *2* (3), 2100089, https://doi.org/10.1002/smsc.202100089. DOI: https://doi.org/10.1002/smsc.202100089 (acccessed 2023/05/16).

(138) Pradas del Real, A. E.; Pérez-Sanz, A.; Lobo, M. C.; McNear, D. H., Jr. The Chromium Detoxification Pathway in the Multimetal Accumulator Silene vulgaris. *Environmental Science & Technology* **2014**, *48* (19), 11479-11486. DOI: 10.1021/es502099g.

(139) Savassa, S. M.; Castillo-Michel, H.; Pradas del Real, A. E.; Reyes-Herrera, J.; Marques, J. P. R.; de Carvalho, H. W. P. Ag nanoparticles enhancing Phaseolus vulgaris seedling development: understanding nanoparticle migration and chemical transformation across the seed coat. *Environmental Science: Nano* **2021**, *8* (2), 493-501, 10.1039/D0EN00959H. DOI: 10.1039/D0EN00959H.

(140) Pradas Del Real, A. E.; Pérez-Sanz, A.; García-Gonzalo, P.; Castillo-Michel, H.; Gismera, M. J.; Lobo, M. C. Evaluating Cr behaviour in two different polluted soils: Mechanisms and implications for soil functionality. *J Environ Manage* **2020**, *276*, 111073. DOI: 10.1016/j.jenvman.2020.111073.

(141) Castillo-Michel, H. A.; Larue, C.; Pradas Del Real, A. E.; Cotte, M.; Sarret, G. Practical review on the use of synchrotron based micro- and nano- X-ray fluorescence mapping and X-ray absorption spectroscopy to investigate the interactions between plants and engineered nanomaterials. *Plant Physiol Biochem* **2017**, *110*, 13-32. DOI: 10.1016/j.plaphy.2016.07.018.

(142) Larue, C.; Castillo-Michel, H.; Stein, R. J.; Fayard, B.; Pouyet, E.; Villanova, J.; Magnin, V.; Pradas del Real, A.-E.; Trcera, N.; Legros, S.; et al. Innovative combination of spectroscopic techniques to reveal nanoparticle fate in a crop plant. *Spectrochimica Acta Part B: Atomic Spectroscopy* **2016**, *119*, 17-24. DOI: https://doi.org/10.1016/j.sab.2016.03.005.

(143) Gödecke, T.; Stein, A. J.; Qaim, M. The global burden of chronic and hidden hunger: trends and determinants. *Global food security* **2018**, *17*, 21-29.

(144) Chen, Y.; Barak, P. Iron nutrition of plants in calcareous soils. *Advances in agronomy* **1982**, *35*, 217-240.

(145) Kim, S. A.; Punshon, T.; Lanzirotti, A.; Li, L.; Alonso, J. M.; Ecker, J. R.; Kaplan, J.; Guerinot, M. L. Localization of Iron in Arabidopsis Seed Requires the Vacuolar Membrane Transporter VIT1. *Science* **2006**, *314* (5803), 1295-1298. DOI: 10.1126/science.1132563 (acccessed 2023/05/28).

(146) Dixon, R.; Cheng, Q.; Shen, G.-F.; Day, A.; Dowson-Day, M. Nif gene transfer and expression in chloroplasts: Prospects and problems. *Plant and Soil* **1997**, *194*, 193-203.

(147) Escudero, V.; Abreu, I.; Tejada-Jiménez, M.; Rosa-Núñez, E.; Quintana, J.; Prieto, R. I.; Larue, C.; Wen, J.; Villanova, J.; Mysore, K. S. Medicago truncatula Ferroportin2 mediates iron import into nodule symbiosomes. *New Phytologist* **2020**, *228* (1), 194-209.

(148) Cesar da Silva, J.; Pacureanu, A.; Yang, Y.; Bohic, S.; Morawe, C.; Barrett, R.; Cloetens, P. Efficient concentration of high-energy x-rays for diffraction-limited imaging resolution. *Optica* **2017**, *4* (5), 492-495. DOI: 10.1364/OPTICA.4.000492.

(149) Cotte, M.; Pouyet, E.; Salomé, M.; Rivard, C.; De Nolf, W.; Castillo-Michel, H.; Fabris, T.; Monico, L.; Janssens, K.; Wang, T.; et al. The ID21 X-ray and infrared microscopy beamline at the ESRF: status and recent applications to artistic materials. *Journal of Analytical Atomic Spectrometry* **2017**, *32* (3), 477-493, 10.1039/C6JA00356G. DOI: 10.1039/C6JA00356G.

(150) Johansson, U.; Carbone, D.; Kalbfleisch, S.; Björling, A.; Kahnt, M.; Sala, S.; Stankevic, T.; Liebi, M.; Rodriguez Fernandez, A.; Bring, B. NanoMAX: the hard X-ray nanoprobe beamline at the MAX IV Laboratory. *Journal of Synchrotron Radiation* **2021**, *28* (6), 1935-1947.

(151) Caplan, J.; Niethammer, M.; Taylor, R. M.; Czymmek, K. J. The power of correlative microscopy: multi-modal, multi-scale, multi-dimensional. *Curr Opin Struct Biol* **2011**, *21* (5), 686-693. DOI: 10.1016/j.sbi.2011.06.010.

(152) Turk, M.; Baumeister, W. The promise and the challenges of cryo-electron tomography. *FEBS Lett* **2020**, *594* (20), 3243-3261. DOI: 10.1002/1873-3468.13948.

(153) *Imaging Modalities for Biological and Preclinical Research: A Compendium, Volume 2*; Walter, A., Mannheim, J. G., Caruana, C. J., Eds.; IOP Publishing, 2021. DOI: 10.1088/978-0-7503-3747-2.

(154) *Imaging Modalities for Biological and Preclinical Research: A Compendium, Volume 1*; Walter, A., Mannheim, J. G., Caruana, C. J., Eds.; IOP Publishing, 2021. DOI: 10.1088/978-0-7503-3059-6.

(155) Domart, F.; Cloetens, P.; Roudeau, S.; Carmona, A.; Verdier, E.; Choquet, D.; Ortega, R. Correlating STED and synchrotron XRF nano-imaging unveils cosegregation of metals and cytoskeleton proteins in dendrites. *Elife* **2020**, *9*. DOI: 10.7554/eLife.62334.

(156) Sanchez-Cano, C.; Romero-Canelón, I.; Yang, Y.; Hands-Portman, I. J.; Bohic, S.; Cloetens, P.; Sadler, P. J. Synchrotron X-Ray Fluorescence Nanoprobe Reveals Target Sites for Organo-Osmium Complex in Human Ovarian Cancer Cells. *Chemistry* **2017**, *23* (11), 2512-2516. DOI: 10.1002/chem.201605911.

(157) Tardillo Suárez, V.; Gallet, B.; Chevallet, M.; Jouneau, P. H.; Tucoulou, R.; Veronesi, G.; Deniaud, A. Correlative transmission electron microscopy and high-resolution hard X-ray fluorescence microscopy of cell sections to measure trace element concentrations at the organelle level. *J Struct Biol* **2021**, *213* (3), 107766. DOI: 10.1016/j.jsb.2021.107766.

(158) Deng, J.; Lo, Y. H.; Gallagher-Jones, M.; Chen, S.; Pryor, A.; Jin, Q.; Hong, Y. P.; Nashed, Y. S. G.; Vogt, S.; Miao, J.; et al. Correlative 3D x-ray fluorescence and ptychographic tomography of frozen-hydrated green algae. *Sci Adv* **2018**, *4* (11), eaau4548. DOI: 10.1126/sciadv.aau4548.

(159) Gramaccioni, C.; Yang, Y.; Pacureanu, A.; Vigano, N.; Procopio, A.; Valenti, P.; Rosa, L.; Berlutti, F.; Bohic, S.; Cloetens, P. Cryo-nanoimaging of Single Human Macrophage Cells: 3D Structural and Chemical Quantification. *Anal Chem* **2020**, *92* (7), 4814-4819. DOI: 10.1021/acs.analchem.9b04096.

(160) Álvarez-Marimon, E.; Castillo-Michel, H.; Reyes-Herrera, J.; Seira, J.; Aso, E.; Carmona, M.; Ferrer, I.; Cladera, J.; Benseny-Cases, N. Synchrotron X-ray Fluorescence and FTIR Signatures for Amyloid Fibrillary and Nonfibrillary Plaques. *ACS Chem Neurosci* **2021**, *12* (11), 1961-1971. DOI: 10.1021/acschemneuro.1c00048.

(161) Mahamid, J.; Pfeffer, S.; Schaffer, M.; Villa, E.; Danev, R.; Cuellar, L. K.; Förster, F.; Hyman, A. A.; Plitzko, J. M.; Baumeister, W. Visualizing the molecular sociology at the HeLa cell nuclear periphery. *Science* **2016**, *351* (6276), 969-972. DOI: 10.1126/science.aad8857.

(162) Dumoux, M.; Glen, T.; Smith, J. L. R.; Ho, E. M. L.; Perdigão, L. M. A.; Pennington, A.; Klumpe, S.; Yee, N. B. Y.; Farmer, D. A.; Lai, P. Y. A.; et al. Cryo-plasma FIB/SEM volume imaging of biological specimens. *Elife* **2023**, *12*. DOI: 10.7554/eLife.83623.

(163) Tegunov, D.; Xue, L.; Dienemann, C.; Cramer, P.; Mahamid, J. Multi-particle cryo-EM refinement with M visualizes ribosome-antibiotic complex at 3.5 Å in cells. *Nat Methods* **2021**, *18* (2), 186-193. DOI: 10.1038/s41592-020-01054-7.

(164) Watanabe, S. Flash-and-Freeze: Coordinating Optogenetic Stimulation with Rapid Freezing to Visualize Membrane Dynamics at Synapses with Millisecond Resolution. *Front Synaptic Neurosci* **2016**, *8*, 24. DOI: 10.3389/fnsyn.2016.00024.

(165) Moore, J.; Basurto-Lozada, D.; Besson, S.; Bogovic, J.; Bragantini, J.; Brown, E. M.; Burel, J. M.; Casas Moreno, X.; de Medeiros, G.; Diel, E. E.; et al. OME-Zarr: a cloud-optimized bioimaging file format with international community support. *bioRxiv* **2023**. DOI: 10.1101/2023.02.17.528834.

(166) Sarkans, U.; Chiu, W.; Collinson, L.; Darrow, M. C.; Ellenberg, J.; Grunwald, D.; Hériché, J.-K.; Iudin, A.; Martins, G. G.; Meehan, T.; et al. REMBI: Recommended Metadata for Biological Images—enabling reuse of microscopy data in biology. *Nature Methods* **2021**, *18* (12), 1418-1422. DOI: 10.1038/s41592-021-01166-8.

(167) Josep, N.; Alessandro, B.; Jordi, J. The Alba ray tracing code: ART. In *Proc.SPIE*, 2013; Vol. 8848, p 88480Z. DOI: 10.1117/12.2024439.

(168) Villar, F.; Andre, L.; Baker, R.; Bohic, S.; da Silva, J. C.; Guilloud, C.; Hignette, O.; Meyer, J.; Pacureanu, A.; Perez, M. Nanopositioning for the ESRF ID16A nano-imaging beamline. *Synchrotron Radiation News* **2018**, *31* (5), 9-14.

(169) Hafizh, I.; Bellotti, G.; Carminati, M.; Utica, G.; Gugiatti, M.; Balerna, A.; Tullio, V.; Borghi, G.; Picciotto, A.; Ficorella, F.; et al. ARDESIA: A fast silicon drift detector X-ray spectrometer for synchrotron applications. *X-Ray Spectrometry* **2019**, *48* (5), 382-386, https://doi.org/10.1002/xrs.3017. DOI: https://doi.org/10.1002/xrs.3017 (acccessed 2023/05/28).

(170) Guijarro, M.; Berruyer, G.; Beteva, A.; Claustre, L.; Coutinho, T.; Dominguez, M.-C.; Guillou, P.; Guilloud, C.; Homs, A.; Meyer, J.; et al. Beamline Experiments at ESRF with BLISS. In *17th International Conference on Accelerator and Large Experimental Physics Control Systems*, New York, United States, 2019-10-05, 2019; p MOCPL03. DOI: 10.18429/JACoW-ICALEPCS2019-MOCPL03.

(171) Könnecke, M.; Akeroyd, F. A.; Bernstein, H. J.; Brewster, A. S.; Campbell, S. I.; Clausen, B.; Cottrell, S.; Hoffmann, J. U.; Jemian, P. R.; Männicke, D.; et al. The NeXus data format. *J Appl Crystallogr* **2015**, *48* (Pt 1), 301-305. DOI: 10.1107/s1600576714027575 From NLM.

(172) Sole, V. A.; Papillon, E.; Cotte, M.; Walter, P.; Susini, J. A multiplatform code for the analysis of energy-dispersive X-ray fluorescence spectra. *Spectrochimica Acta Part B: Atomic Spectroscopy* **2007**, *62* (1), 63-68. DOI: https://doi.org/10.1016/j.sab.2006.12.002.

(173) Mirone, A.; Brun, E.; Gouillart, E.; Tafforeau, P.; Kieffer, J. The PyHST2 hybrid distributed code for high speed tomographic reconstruction with iterative reconstruction and a priori knowledge capabilities. *Nuclear Instruments and Methods in Physics Research Section B: Beam Interactions with Materials and Atoms* **2014**, *324*, 41-48. DOI: https://doi.org/10.1016/j.nimb.2013.09.030.

(174) Langer, M.; Zhang, Y.; Figueirinhas, D.; Forien, J.-B.; Mom, K.; Mouton, C.; Mokso, R.; Villanueva-Perez, P. PyPhase–a Python package for X-ray phase imaging. *Journal of Synchrotron Radiation* **2021**, *28* (4), 1261-1266.

(175) Gh Popescu, B. F.; Nichol, H. Mapping Brain Metals to Evaluate Therapies for Neurodegenerative Disease. *CNS Neuroscience & Therapeutics* **2011**, *17* (4), 256-268, https://doi.org/10.1111/j.1755-5949.2010.00149.x. DOI: https://doi.org/10.1111/j.1755-5949.2010.00149.x (acccessed 2023/05/28).

(176) Grochowski, C.; Blicharska, E.; Krukow, P.; Jonak, K.; Maciejewski, M.; Szczepanek, D.; Jonak, K.; Flieger, J.; Maciejewski, R. Analysis of Trace Elements in Human Brain: Its Aim, Methods, and Concentration Levels. *Frontiers in Chemistry* **2019**, *7*, Review. DOI: 10.3389/fchem.2019.00115.

(177) Townsend, O.; Gazzola, S.; Dolgov, S.; Quinn, P. Undersampling raster scans in spectromicroscopy for a reduced dose and faster measurements. *Opt Express* **2022**, *30* (24), 43237-43254. DOI: 10.1364/oe.471663 From NLM.

(178) Gao, Z.; Odstrcil, M.; Böcklein, S.; Palagin, D.; Holler, M.; Ferreira Sanchez, D.; Krumeich, F.; Menzel, A.; Stampanoni, M.; Mestl, G.; et al. Sparse ab initio x-ray transmission spectrotomography for nanoscopic compositional analysis of functional materials. *Sci Adv* **2021**, *7* (24). DOI: 10.1126/sciadv.abf6971 From NLM.

(179) Lauzier, P. T.; Chen, G. H. Characterization of statistical prior image constrained compressed sensing (PICCS): II. Application to dose reduction. *Med Phys* **2013**, *40* (2), 021902. DOI: 10.1118/1.4773866 From NLM.

(180) Fernandez-Carreiras, D.; Beltran, D.; Coutinho, T.; Cuni, G.; Klora, J.; Matilla, O.; Montano, R.; Pascual-Izarra, C.; Puso, S.; Ranz, R.; et al. The design of the Alba control system: a cost-effective distributed hardware and software architecture. In *Contributions to the Proceedings of ICALEPCS 2011*, France, 2012; p 1423.

(181) Peddie, C. J.; Genoud, C.; Kreshuk, A.; Meechan, K.; Micheva, K. D.; Narayan, K.; Pape, C.; Parton, R. G.; Schieber, N. L.; Schwab, Y.; et al. Volume electron microscopy. *Nature Reviews Methods Primers* **2022**, *2* (1), 51. DOI: 10.1038/s43586-022-00131-9.

(182) Du, M.; Jacobsen, C. Relative merits and limiting factors for x-ray and electron microscopy of thick, hydrated organic materials. *Ultramicroscopy* **2018**, *184* (Pt A), 293-309. DOI: 10.1016/j.ultramic.2017.10.003 From NLM.

(183) Kak, A. C.; Slaney, M. *Principles of computerized tomographic imaging*; SIAM, 2001.

(184) Meechan, K.; Guan, W.; Riedinger, A.; Stankova, V.; Yoshimura, A.; Pipitone, R.; Milberger, A.; Schaar, H.; Romero-Brey, I.; Templin, R. Crosshair, semi-automated targeting for electron microscopy with a motorised ultramicrotome. *Elife* **2022**, *11*, e80899.

(185) Holler, M.; Ihli, J.; Tsai, E. H.; Nudelman, F.; Verezhak, M.; van de Berg, W.; Shahmoradian, S. H. A lathe system for micrometre-sized cylindrical sample preparation at room and cryogenic temperatures. *Journal of synchrotron radiation* **2020**, *27* (2), 472-476.

(186) Bosch, C.; Lindenau, J.; Pacureanu, A.; Peddie, C. J.; Majkut, M.; Douglas, A. C.; Carzaniga, R.; Rack, A.; Collinson, L.; Schaefer, A. T. Femtosecond laser preparation of resin embedded samples for correlative microscopy workflows in life sciences. *Applied Physics Letters* **2023**, *122* (14), 143701.